Development 135, 1137-1146 (2008) doi:10.1242/dev.012062

Precision of the Dpp gradient

Tobias Bollenbach[1,*,†], Periklis Pantazis[2,*,‡], Anna Kicheva[2,3,*], Christian Bökel[2,§], Marcos González-Gaitán[2,3,¶] and Frank Jülicher[1,¶]

Morphogen concentration gradients provide positional information by activating target genes in a concentration-dependent manner. Recent reports show that the gradient of the syncytial morphogen Bicoid seems to provide precise positional information to determine target gene domains. For secreted morphogenetic ligands, the precision of the gradients, the signal transduction and the reliability of target gene expression domains have not been studied. Here we investigate these issues for the TGF-β-type morphogen Dpp. We first studied theoretically how cell-to-cell variability in the source, the target tissue, or both, contribute to the variations of the gradient. Fluctuations in the source and target generate a local maximum of precision at a finite distance to the source. We then determined experimentally in the wing epithelium: (1) the precision of the Dpp concentration gradient; (2) the precision of the Dpp signaling activity profile; and (3) the precision of activation of the Dpp target gene *spalt*. As captured by our theoretical description, the Dpp gradient provides positional information with a maximal precision a few cells away from the source. This maximal precision corresponds to a positional uncertainly of about a single cell diameter. The precision of the Dpp gradient accounts for the precision of the *spalt* expression range, implying that Dpp can act as a morphogen to coarsely determine the expression pattern of target genes.

KEY WORDS: *Drosophila*, Morphogen, Precision, Wing imaginal disk

INTRODUCTION

Morphogens form graded concentration profiles in target tissues adjacent to a region of secreting cells (reviewed by Tabata and Takei, 2004). It has been suggested that morphogen gradients pattern developing tissues by providing positional information to the target cells by means of the concentration-dependent expression of target genes (Wolpert, 1969). Prominent examples of morphogens are Bicoid (Bcd), which acts in the *Drosophila* embryo (Driever and Nüsslein-Volhard, 1988a; Driever and Nüsslein-Volhard, 1988b), Decapentaplegic (Dpp), which also acts in the *Drosophila* wing disk (Entchev et al., 2000; Teleman and Cohen, 2000), and Activin in the *Xenopus* embryo (Gurdon et al., 1994).

The question of whether morphogen gradients can precisely guide the patterning of growing tissues has deserved attention in recent years. In particular, a number of studies have addressed the precision of the Bcd gradient, which specifies the expression domain positions of gap genes, such as *hunchback* (*hb*), *Krüppel* and *giant*, in the early *Drosophila* embryo (Bergmann et al., 2007; Crauk and Dostatni, 2005; Gregor et al., 2005; Gregor et al., 2007; Houchmandzadeh et al., 2002; Houchmandzadeh et al., 2005; Jaeger et al., 2004). These domains are established while the embryo is still a syncytium, i.e. the nuclei are not separated by cell membranes. In the context of the positional information paradigm, the Bcd gradient has been scrutinized for its ability to define by itself the precise domain of *hb* and its variability from embryo to embryo. A recent report shows that the shape of the Bcd gradient leads to relative concentration differences between neighboring cells of about 10%. This is also the concentration variability at corresponding positions in multiple embryos and the relative magnitude of the noise in readout of Bcd by the activation of *hb* (Gregor et al., 2007). Together, these observations suggest that the system exerts precise control over the absolute Bcd concentrations and responds reliably to small concentration differences.

The issue of precision also arises for morphogens that form graded profiles in fields of cells rather than a syncytium. In these fields, individual cells have slightly different sizes, shapes, number of receptors and other properties. As a consequence of this cell-to-cell variability, morphogens form concentration profiles that are overall graded, but which exhibit fluctuations on shorter length scales. Here, we study the Dpp morphogen gradient in the *Drosophila* wing disk. Dpp signaling is initiated by Dpp binding to its heterodimeric receptors, after which the type I receptor, Thickveins, phosphorylates the R-Smad, Mothers against Dpp (Mad) (Kim et al., 1997; Newfeld et al., 1997). Phosphorylated Mad (PMad), after binding to the co-Smad Medea, translocates to the nucleus. There it represses directly the transcription of the transcriptional repressor Brinker (Campbell and Tomlinson, 1999; Jazwinska et al., 1999; Moser and Campbell, 2005; Müller et al., 2003) (reviewed by Affolter and Basler, 2007), which therefore forms a gradient inverse to that of Dpp, and ultimately leads to the determination of the boundaries of Dpp target genes, such as *spalt* (*sal*; also known as *spalt major*) (Kühnlein et al., 1994; Barrio and de Celis, 2004).

A number of features distinguish the Bcd from the Dpp gradient: Bcd operates in a syncytium and Dpp in a field of cells; Bcd spreads within a field of fixed size and Dpp in a growing tissue; the Bcd gradient is likely to be read out before the steady state is reached (Bergmann et al., 2007), whereas the Dpp readout might occur at all stages of development.

[1]Max-Planck-Institute for the Physics of Complex Systems, Nöthnitzer Strasse 38, 01187 Dresden, Germany. [2]Max-Planck-Institute of Molecular Cell Biology and Genetics, Pfotenhauer Strasse 108, 01307 Dresden, Germany. [3]Department of Biochemistry, Sciences II, 30 Quai Ernest-Ansermet, 1211 Geneva 4, Switzerland.

*These authors contributed equally to this work
†Present address: Department of Systems Biology, Harvard Medical School, 200 Longwood Avenue, Boston, MA 02115, USA
‡Present address: California Institute of Technology, 1200 E. California Blvd., Pasadena, CA 91125, USA
§Present address: DFG Center for Regenerative Therapies, Tatzberg 47-49, 01307 Dresden, Germany
¶Authors for correspondence (e-mails: marcos.gonzalez@biochem.unige.ch; julicher@pks.mpg.de)

Accepted 24 December 2007

Combining the fluorescence profiles of GFP-Dpp (Entchev et al., 2000) in a large dataset, we analyze the Dpp concentration fluctuations as a function of the distance from the source. We interpret the behavior of these fluctuations using a theoretical description of morphogen production, transport and degradation, which represents cell-to-cell variability in the target and source regions by random variations of the effective diffusion coefficient, the effective degradation rate and the Dpp production rate. We compare the precision of the Dpp gradient to that of the nuclear concentration of PMad, as an indicator of Dpp signaling activity. Finally, we investigate the relationship between the Dpp concentration fluctuations, the precision of the expression domain of the target gene *spalt* and that of the final morphological vein pattern.

MATERIALS AND METHODS

Transgenic strains, immunostaining and imaging

Genotypes: dpp^{d8}/dpp^{d12}; *dppGal4/UAS-GFP-Dpp*. $In(2L)dpp^{d8}$ and $In(2L)dpp^{d12}$ are described in FlyBase; *UAS-GFP-Dpp* has been described previously (Entchev et al., 2000). Third-instar larvae that developed for the same time under the same conditions at 25°C were used. Wing disks were immunostained and prepared as previously described (Entchev et al., 2000; Kicheva et al., 2007). Antibodies: mouse anti-Patched (Capdevila et al., 1994) 1:200 dilution; rabbit anti-Spalt (Kühnlein et al., 1994) 1:50; rat anti-Spalt (de Celis et al., 1999) 1:600; rabbit anti-PMad (Tanimoto et al., 2000) 1:1000; secondary Alexa-546 and -633 conjugated (Molecular Probes) 1:500.

Vein patterns in the adult wing

We quantified 88 wild-type male and female adult wings. We first drew a line connecting the two ends of vein L4. Through this line, we drew a perpendicular line closest to the position where vein L4 crosses the posterior crossvein. This line is delimited by the wing margin and defines the anterior-posterior length of the wing. We defined the distance between veins L2 and L3 as the segment of the anterior-posterior length that lies between veins L2 and L3.

Data analysis

We analyzed 30 GFP-Dpp gradients in 15 third-instar wing disks. The average fluorescence intensity (FI) in a 3.1 μm square was measured in the middle of the dorsal and ventral compartments at continuously varying distances to the source from an additive projection of 15 *z*-sections (1 μm apart) using ImageJ (http://rsb.info.nih.gov/ij/) (Fig. 4A). The source boundary was determined using the abrupt decrease of PMad fluorescence in the source cells (Fig. 4B). Background FI (the lowest FI value far away from the source) was subtracted. The FI profiles were normalized to the total FI I^{Dpp} defined as the integral over each profile (Fig. 4C). $\sigma_c^{\mathrm{Dpp}}(x)$ and $\Sigma^{\mathrm{Dpp}}(x)$ were averaged in *x*-bins of 3.1 μm for Fig. 4E,F, and 2.5 μm for Fig. 5F. Error bars in Fig. 4E,F are twice the standard deviation of σ_c^{Dpp} and Σ^{Dpp} in each bin, respectively.

For the PMad gradients (Fig. 5B), the maximum intensity c_i^{PMad} in one *z*-slice (width 1.8 μm) was measured for each individual nucleus *i* at a respective distance from the source x_i in the central third of the dorsal and ventral parts of the posterior compartment using Metamorph (Universal Imaging Corporation). The profiles were normalized to the total FI I^{PMad}, i.e. the integral over the curve that linearly interpolates between the c_i^{PMad} in the anterior to posterior direction. Background fluorescence (measured outside the range of the Dpp signal) was subtracted before normalization. σ_c^{Pmad} was calculated in *x* bins of 2.5 μm via $\sigma_c^{\mathrm{Pmad}}=(\Sigma_{i=1}^{N}(c_i^{\mathrm{PMad}}-\bar{c}_i^{\mathrm{Pmad}}(x_i))^2/\mathrm{N})^{1/2}$ where $\bar{c}_i^{\mathrm{PMad}}(x)=P_0\exp(-x/\lambda^{\mathrm{PMad}})$ is the exponential fit to the PMad concentration profile and the sum extends over all *N* nuclei located in each bin.

The *sal*-expression domain was analyzed the same way as the GFP-Dpp profiles (Fig. 6A). The *sal* range was determined by fitting the sigmoidal function $s(x)=s_0(\tanh((d-x)/w)+1)/2$ to each profile using s_0, *d* and *w* as fit parameters. The distance $x^*=d+w$ corresponds to the *sal* range.

All fits were performed using the nonlinear least-squares Marquardt-Levenberg algorithm (Mathematica 5.2, Wolfram Research). We estimated the disk sizes *L* as the linear extension of the GFP-Dpp source (Fig. 4A). The average cell diameter was estimated from the average area of a cell (5.46±0.82 μm, n=1200 cells), assuming that the cell is a circle.

Theoretical description of morphogen gradient precision

We discuss a simple model of morphogen gradient formation based on non-directional transport, characterized by an effective diffusion coefficient D, and degradation with an effective degradation rate k. Morphogens secreted in the source ($x<0$) enter the tissue with a current j at the boundary line $x=0$ of the two-dimensional target area (Fig. 1A,B) (see also Kruse et al., 2004; Lander et al., 2002). Cell-to-cell variability implies that the efficiency of transport and degradation vary at different positions. We consider this by assuming that D and k are functions of the position $\bar{x}=(x,y)$, with $D(\bar{x})=D_0+\eta(\bar{x})$ where D_0 is the average diffusion coefficient and $\eta(\bar{x})$ is a random function with zero average that describes the fluctuations. Analogously, we define $k(\bar{x})=k_0+\zeta(\bar{x})$.

Fig. 1C illustrates this model in one dimension. In a continuum limit, it can be described by

$$\frac{\partial}{\partial t}c(t,\bar{x})=\nabla\cdot\left[(D_0+\eta(\bar{x}))\nabla c(t,\bar{x})\right]-(k_0+\zeta(\bar{x}))c(t,\bar{x})\,, \qquad (1)$$

where $\nabla=(\partial/\partial x,\partial/\partial y)$. Production rate fluctuations in the source are captured by a boundary condition $j(\bar{x})=j_0+\chi(\bar{x})|_{x=0}$ on the current at $x=0$, where j_0 is the average current across this boundary and $\chi(\bar{x})|_{x=0}$ is a random function with zero average.

Equation (1) is closely related to the well-known diffusion equation with degradation term, but includes cell-to-cell variability. In steady state, equation (1) leads to a graded concentration profile $c(\bar{x})$ for each realization of the random variables $\eta(\bar{x})$, $\zeta(\bar{x})$ and $\chi(\bar{x})|_{x=0}$. Owing to the presence of multiplicative noise in equation (1), the analytical calculation of the steady-state solution is challenging. To calculate the first-order correction to the noiseless case, we used a field theoretic perturbation expansion in the noise strength. This allows us to express the concentration fluctuations in terms of Green's functions and the fluctuation amplitudes of D, k and j. A detailed theoretical study is included in the supplementary material.

We can estimate the precision of the positional information conveyed by the gradient. If the target position x^* is defined by a threshold concentration c^* where $c(x^*)=c^*$, the fluctuations of $c(x)$ generate an uncertainty

$$\sigma_x^*=\left\langle(x^*-\bar{x}^*)^2\right\rangle^{1/2}\cong\frac{-\sigma_c(x^*)}{\partial_x\bar{c}(x)\,|_{x=x^*}} \qquad (2)$$

of x^* where $\bar{x}^*=\langle x^*\rangle$ is the average value of the target position, $\bar{c}(x^*)=\langle c(\bar{x})|_{x=x^*}\rangle$ is the average concentration at x^*, and $\sigma_c(x^*)=\langle(c(\bar{x})|_{x=x^*}-\bar{c}(x^*))^2\rangle^{1/2}$ is the concentration uncertainty at x^* (Fig. 4D). The average steady-state gradient that results from (1) is given by an exponential decay, $\bar{c}(x)=c_0\exp(-x/\lambda)$ with $\lambda=\sqrt{D_0/k_0}$. One can thus express the uncertainty defined in (2) as

$$\sigma_x^*\cong\lambda\Sigma(x^*)\,, \qquad (3)$$

where $\Sigma(x^*)=\sigma_c(x^*)/\bar{c}(x^*)$. This reveals a direct relationship between the uncertainty of the threshold position x^* and $\Sigma(x^*)$.

RESULTS

Theoretical study of morphogen gradient fluctuations

We first asked what is at the origin of morphogen concentration fluctuations observed in an epithelium such as the wing disk. Individual cells can differ in size, shape, number of receptors and protein transport rates (Fig. 1A). This cell-to-cell variability affects morphogen transport, degradation, production and storage in endosomes and thus induces spatial variations in the resulting concentration profile (Fig. 1B). Cell-to-cell variability has been reported within various systems (Arias and Hayward, 2006;

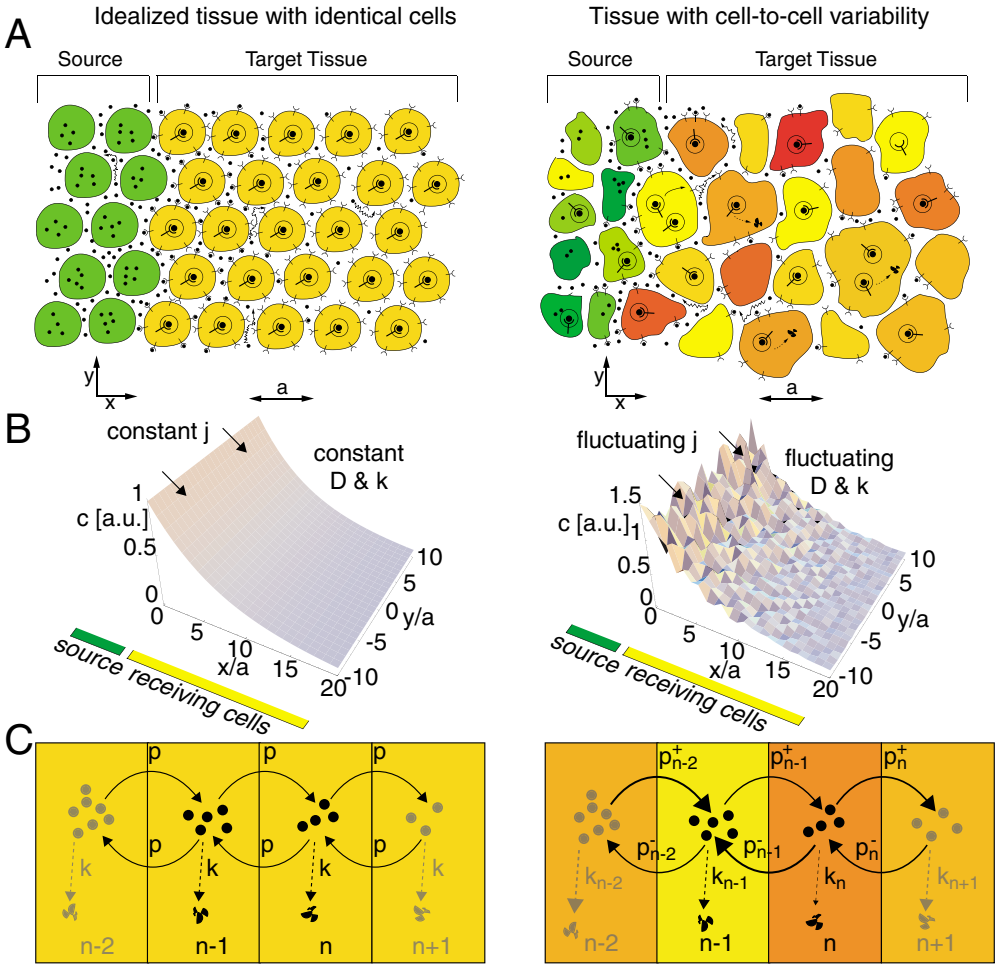

Fig. 1. Morphogen gradient formation in the presence of cell-to-cell variability. (**A**) Cellular individuality in the wing disk. The stochastic concentrations of intracellular and extracellular molecules and different cell shapes affect morphogen transport and degradation, independently of the transport mechanism. (**B**) Gradient formation in a simplified geometry. Concentration profiles for constant (left) or fluctuating (right) morphogen influx j, effective D and k. Average cell diameter, a. (**C**) One-dimensional lattice model of the scenarios in A. The hopping rates p^+_n and p^-_n describe transport between cells n and n+1. They fluctuate about their mean value p_0 because of cell-to-cell variability, as indicated by arrows of different widths. The degradation rate k_n also fluctuates.

Colman-Lerner et al., 2005; Elowitz et al., 2002; Raser and O'Shea, 2005). In the following, we discuss the impact of such variability on morphogen gradients.

Several theoretical descriptions of gradient formation have been developed (Bollenbach et al., 2005; Eldar et al., 2002; Eldar et al., 2003; Howard and ten Wolde, 2005; Kruse et al., 2004; Lander et al., 2002). Here, we use an effective description of non-directional morphogen transport, independent of the specific underlying mechanisms [restricted extracellular diffusion or planar transcytosis (Bollenbach et al., 2007; González-Gaitán, 2003; Strigini, 2005)]. Morphogen transport can be characterized by the influx j of morphogens into the target tissue, an effective diffusion coefficient D, and a degradation rate k. Using a fluorescence recovery after photobleaching (FRAP) assay, we have recently measured these parameters (j, D and k) in a manner independent of the microscopic transport mechanism (Kicheva et al., 2007). The effective diffusion coefficient could correspond to passive extracellular diffusion or transcytosis (Bollenbach et al., 2005). Similarly, the effective degradation rate can be affected by extracellular proteolytic degradation or lysosomal degradation. Finally, morphogen secretion from the source determines the influx j.

In our description of morphogen transport, we consider cell-to-cell variability by introducing spatial fluctuations of the parameters D, k and j (Fig. 1). In an ensemble of gradients, this leads to an average steady-state concentration profile of the form $\bar{c}(x)=C_0\exp(-x/\lambda)$ where x denotes the distance from the source (Fig. 1B), C_0 is the average concentration directly adjacent to the source, and λ is the gradient decay length, i.e. the length over which the concentration decreases by a factor of e. At each position x, concentration fluctuations about this average profile are characterized by the standard deviation of the concentration $\sigma_c(x)$. To characterize the fluctuations of the gradient, we study the 'relative concentration uncertainty' $\Sigma(x)=\sigma_c(x)/\bar{c}(x)$, which quantifies concentration fluctuations irrespective of the absolute value of the local average concentration.

It has been proposed that morphogen gradients provide positional information by activating target genes above distinct concentration thresholds that occur at precise distances from the source (Wolpert, 1969). In this scenario, the relevant quantity is the precision of the distance from the source at which a particular morphogen concentration occurs. This is captured by the 'positional uncertainty' $\sigma_x=\langle(x(c)-\bar{x}(c))^2\rangle^{1/2}$, i.e. the standard deviation of the position x, carrying a given concentration c. The positional uncertainty σ_x at a position x can be determined from the relative concentration uncertainty Σ at this position via $\sigma_x(x)\cong\lambda\Sigma(x)$ (see Materials and methods). The precision of the gradient is inversely related to σ_x. We obtained analytical expressions for the gradient precision, which were verified numerically (see the theoretical study in the supplementary material).

Source versus target tissue variability: effect on precision

The effects of fluctuations can be discussed systematically by considering two simplified situations: (1) cell-to-cell variations exist only in the source and (2) they exist only in the target tissue. The real

situation in the wing disk is the combination of both. We first consider the hypothetical case in which there is cell-to-cell variability in the source, whereas the target cells are identical (Fig. 2A). In this case, the influx j fluctuates along the source boundary, while D and k in the target tissue are constant. Our analysis shows that the fluctuations of j along the source boundary lead to an uncertainty of the morphogen concentration in the target tissue that decreases away from the source (Fig. 2B). This decrease results from the fact that morphogens that arrive far from the source originate from many different source cells, and from fewer source cells near the source. At large distances, the concentration has low uncertainty because it results from an average over the production rates of many source cells. In a two-dimensional epithelium, $\Sigma(x)$ resulting from variations of j decreases following the power-law $\Sigma(x)\sim x^{-1/4}$ for large distances x (see continuum limit in the supplementary material).

In the second case, in which producing cells are identical, whereas there is variability in the target (Fig. 2C), the influx j is constant while D and k fluctuate. Our analysis reveals a sudden decrease in $\Sigma(x)$ in the region abutting the source, followed by a monotonic increase at larger distances (Fig. 2D). This increasing uncertainty results from an accumulation of fluctuations as the concentration profile forms at increasing distances from the source. In a two-dimensional tissue, the concentration uncertainty increases as the power-law $\Sigma(x)\sim x^{1/4}$ for large distances x (see continuum limit and Fig. S3 in the supplementary material).

In general, cell-to-cell variability exists both in the source and the target tissue. In this general scenario, $\Sigma(x)$ first decreases for small distances from the source, reaches a minimum, and then increases for large x (Fig. 2E).

In this analysis, fluctuations of the three trafficking parameters (D, k and j) are uncorrelated. If both diffusion and degradation rely on the same cellular machineries – e.g. if morphogen transport and degradation are mediated by intracellular trafficking (Entchev et al., 2000) – the effective diffusion coefficient and the degradation rate could be correlated. We found that positively correlated fluctuations in D and k lead to reduced concentration uncertainty (see Figs S1,

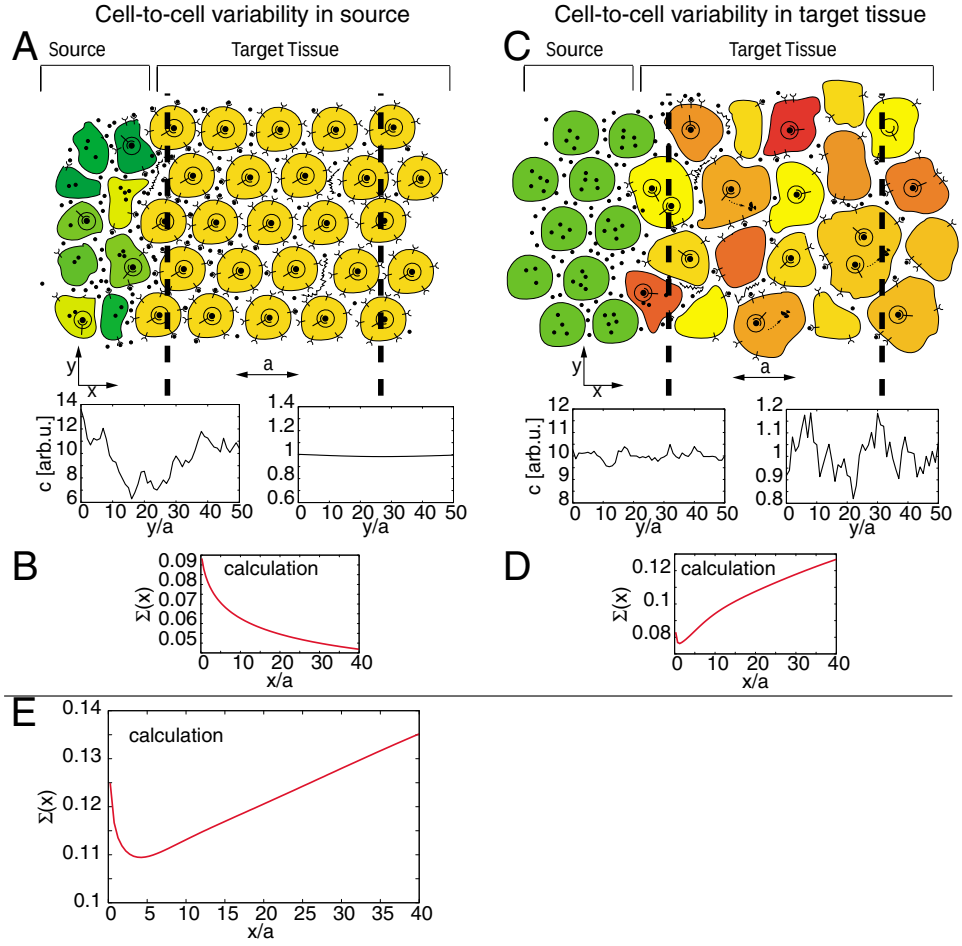

Fig. 2. Cell-to-cell variability in the source or target affects the gradient fluctuations differently. (**A**) Idealized situation with fluctuating production rate in the source (different colors), but identical target cells. Morphogen concentration c along a slice (dashed line) in the y-direction close to the source (bottom left), and at a larger distance from the source (bottom right). (**B**) Theoretical $\Sigma(x)$ for the situation in A based on the model in Fig. 1C in two dimensions. Here, j fluctuates, while D and k are constant. $\Sigma(x)$ decreases with increasing distance x from the source, as in A. (**C**) The opposite situation to A: different target cells, identical source. (**D**) Calculation corresponding to C based on the model in Fig. 1C in two dimensions. D and k fluctuate, j is constant. Following an abrupt decrease very close to the source, $\Sigma(x)$ increases with increasing x. (**E**) $\Sigma(x)$ when cell-to-cell variability affects both the source and the target, i.e. with fluctuating j, D and k. The effects in A and C are superimposed. A pronounced minimum of $\Sigma(x)$ at a finite distance from the source occurs. Whereas its location and the magnitude of $\Sigma(x)$ depend on parameter choice, the qualitative behavior of the curve is independent of these parameters for different noise intensities of the same order of magnitude. Parameters in B,D,E are $\lambda_D/a=7$, $\sigma_D/D_0=1$, $\sigma_k/k_0=1$, $\sigma_j/j_0=0.37$ (for details, see continuum limit and Fig. S2 in the supplementary material).

S2 in the supplementary material). In addition to cell-to-cell variability within one disk, certain parameters may vary from disk-to-disk. In particular, this appears to be so for the morphogen secretion rate (see below). We consequently studied the effects of such disk-to-disk variations of secretion in our theoretical description. These variations increase the relative concentration uncertainty and render its minimum less pronounced (see Fig. S4 in the supplementary material).

Effect of geometry on precision

We then generalized the theory of gradient precision for developmental contexts other than the two-dimensional epithelium. Indeed, morphogen gradients also form in one-dimensional chains of cells such as the mandibular arch in zebrafish (Kimmel et al., 2003) or three-dimensional tissues such as the ventral neural tube in which the sonic hedgehog gradient forms during vertebrate nervous system development (Ericson et al., 1996) (reviewed by Briscoe and Ericson, 1999) (Fig. 3A-C). In one dimension, a given fluctuation – e.g. a transport deficiency in some cell – affects the steady-state concentration profile at all positions farther away because all molecules moving from the source have to pass the deficient cell (Fig. 3A). In two dimensions, this effect is weaker because the morphogens can reach any position on many different paths through the tissue (Fig. 3B). Analogously, the impact of cell-to-cell variability is even weaker in three dimensions (Fig. 3C). Our calculations confirm these ideas: higher tissue dimensionality leads to a strong reduction of the concentration uncertainty $\Sigma(x)$ (Fig. 3D).

At large distances from the source, the concentration uncertainty obeys general power-laws $\Sigma(x)\sim x^{\nu}$ as described above for the two-dimensional scenario. The exponent ν depends on the dimensionality d of the tissue and is given by $\nu=(3-d)/4$ if $d<3$. For $d=3$ the exponent $\nu=0$, which implies an uncertainty that does not increase with increasing distance from the source. Further analysis in this case reveals that there remains a weak logarithmic increase $\Sigma(x)\sim\ln(x)$ for large x. These behaviors also hold if fluctuations only occur in the target, whereas the source does not fluctuate. However, if fluctuations occur only in the source, the concentration uncertainty in the target obeys the power-law $\Sigma(x)\sim x^{(1-d)/4}$ for large x.

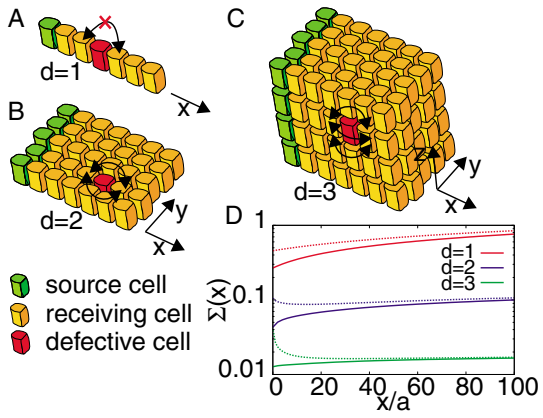

Fig. 3. Role of tissue dimensionality for morphogen gradient precision. (**A**) In a one-dimensional chain of cells, morphogens cannot get beyond the defective cell (red), resulting in a large impact on the gradient. (**B**) In two-dimensional tissues, the effect of one defective cell is smaller because it can be bypassed (arrows) if morphogen transport is non-directional. (**C**) In three-dimensional tissues, the effect is even smaller because there are more paths to bypass the defective cell. (**D**) Logarithmic plot of theoretical $\Sigma(x)$ calculated for different dimensions, but otherwise identical parameters. Only the target cells are subject to cell-to-cell variability (solid lines), or both the source and the receiving cells (dashed lines). $\lambda_D/a=7$, $\sigma_D/D_0=0$, $\sigma_k/k_0=1$, $\sigma_j/j_0=0.37$ (for details, see Fig. S3 in the supplementary material).

Precision of the Dpp gradient in the *Drosophila* wing disk

Our theoretical framework to describe morphogen gradient precision enables us to determine experimentally the precision of the Dpp gradient in the *Drosophila* wing disk and to test our theoretical prediction that $\Sigma(x)$ decreases for small values of the distance x from the source and increases for larger x (Fig. 2E). To analyze the Dpp gradient precision, we determined the shapes of 30 Dpp profiles from third-instar larvae. Using a GFP-Dpp fusion protein in a *dpp* mutant background (see Materials and methods) (Entchev et al., 2000), we measured the GFP fluorescence intensity (FI) as a function of the distance to the Dpp source in the posterior compartments (Fig. 4A-C, Materials and methods). Recently, we have calibrated FI to GFP-Dpp concentration (Kicheva et al., 2007) using GFP-tagged rotavirus-like particles (Charpilienne et al., 2001). Our analysis showed that we can reliably detect differences in concentration of less than 2% of the GFP-Dpp concentration close to the source. This allows us to undertake a quantitative analysis of the gradient and its variability.

Indeed, the gradient shape varies from disk to disk (Fig. 4C), as does the overall level of fluorescence [variation coefficient 0.26 (standard deviation relative to mean)]. We determined the average FI profile $\bar{c}^{Dpp}(x)=\langle c^{Dpp}(x)\rangle$ and its standard deviation $\sigma_c^{Dpp}(x)=\langle(c^{Dpp}(x)-\bar{c}^{Dpp}(x))^2\rangle^{1/2}$ (Fig. 4C-E, details in Materials and methods). The shape of individual gradients is well described by an exponential decay $c^{Dpp}(x)\cong C_0\exp(-x/\lambda^{Dpp})$ (red line in Fig. 4D) with an average decay length $\lambda^{Dpp}=17.0\pm4.3$ μm=6.5±1.7 cells (see Table S1 in the supplementary material) and variable fluorescence levels at the source boundary, C_0 (Kicheva et al., 2007). This value of λ^{Dpp} implies that neighboring cells (with diameter 2.6 μm) experience Dpp concentrations that differ on average by 15%, similar to the 10% difference in the case of Bcd in the syncytial blastoderm (Gregor et al., 2007). We determined C_0 and λ^{Dpp} for each GFP-Dpp profile by a fit to the function $C_0\exp(-x/\lambda^{Dpp})$. We find that λ^{Dpp} is not correlated with the wing disk size L, defined as the dorsal-ventral extension of the source in the wing pouch (Fig. 4A; see Table S2 in the supplementary material). The standard deviation $\sigma_c^{Dpp}(x)$ decreases with increasing distance to the source (Fig. 4E). This is partially because the average concentration decays away from the source. To measure the gradient fluctuations, we therefore investigated the relative concentration uncertainty $\Sigma^{Dpp}(x)=\sigma_c^{Dpp}(x)/\bar{c}^{Dpp}(x)$. Close to the source, $\Sigma^{Dpp}(x)$ decreases for a few cell diameters until it reaches a minimal value at about x=4 μm, and increases monotonously distally for larger distances from the source (Fig. 4F).

As discussed above, we can determine the positional uncertainty $\sigma_x^{Dpp}(x)$ of the Dpp gradient at a position x from $\Sigma^{Dpp}(x)$ using $\sigma_x^{Dpp}(x)\cong\lambda^{Dpp}\Sigma^{Dpp}(x)$ (Materials and methods). We find that, at its minimum 4 μm from the source, the positional uncertainty of the Dpp gradient is smaller than two cell diameters [$\sigma_x^{Dpp}(4\ \mu m)\cong4.4$ μm =1.7 cells]. Next to the source, $\sigma_x^{Dpp}(1\ \mu m)\cong6.0$ μm =2.3 cells, whereas at 40 μm from the source, a distance at around which the Dpp gradient has been proposed to position target gene boundaries [e.g. *sal* and *omb* (also known as *bifid*)], $\sigma_x^{Dpp}(40\ \mu m)\cong9.7$ μm=3.7 cells.

We have so far presented our analysis based directly on the GFP-Dpp FI profiles that we measured. To separate the variations of the gradient shape from overall FI variations between different

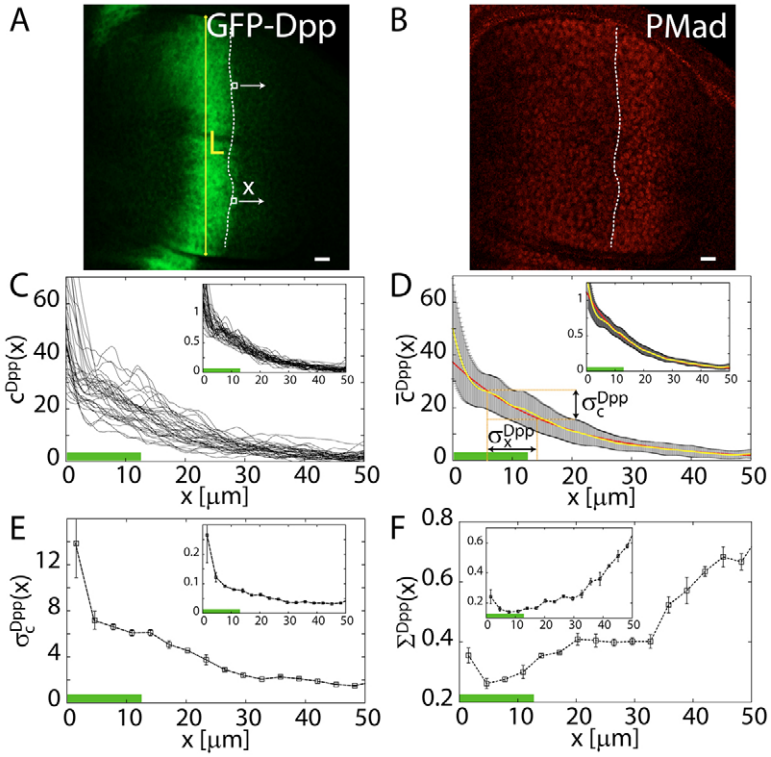

Fig. 4. Fluctuations of the GFP-Dpp gradient in the absence of endogenous Dpp for 30 gradients. Genotype: *dpp^{d8}/dpp^{d12}; dppGal4/UAS-GFP-Dpp.* (**A**,**B**) GFP-Dpp gradient (A, green) and PMad immunostaining (B, red) to identify the source boundary (dotted line), located at x=0 in C-F. Disk size L (yellow line). The white box indicates the square which is scanned to perform the measurement. Scale bars: 10 μm. Posterior, right. (**C**) GFP-fluorescence intensity (FI) $c^{Dpp}(x)$ in the white squares shown in A as a function of the distance to the source. Two profiles (in the dorsal and ventral compartments) were recorded per disk. (**D**) Mean FI $\bar{c}^{Dpp}(x)$ at each position (yellow line) with error bars (black region surrounding the yellow line) showing the standard deviation. Red line, fit of the function $C_0\exp(-x/\lambda^{Dpp})$ to the mean profile. The uncertainty σ_c^{Dpp} of the FI leads to an uncertainty σ_x^{Dpp} of the position where this FI is present. (**E**) Standard deviation $\sigma_c^{Dpp}(x)$ of the FI. (**F**) Relative uncertainty $\Sigma^{Dpp}(x)=\sigma_c^{Dpp}(x)/\bar{c}^{Dpp}(x)$ of the FI for the ensemble of gradients. Note the qualitative similarity to Fig. 2E. Insets in C-F show corresponding results for the normalized Dpp profiles. Green horizontal bars in C-F, 5 cell diameters (13 μm).

disks, we normalized the fluorescence to the total intensity I^{Dpp} in the posterior compartment of each disk (see Materials and methods, Fig. 4C-F insets). The analysis of the normalized data captures the effects of local cellular fluctuations on the gradient precision, by ignoring global variations between different disks. Next to the source, we find $\sigma_x^{Dpp}(1\ \mu m)\cong 4.1\ \mu m = 1.6$ cells, and 40 μm away $\sigma_x^{Dpp}(40\ \mu m)\cong 6.1\ \mu m = 2.3$ cells. As in our theory, the minimum of $\Sigma^{Dpp}(x)$, corresponding to $\sigma_x^{Dpp}(9\ \mu m)\cong 2.4\ \mu m = 0.9$ cells, is more pronounced and the gradient precision is higher if we normalize and study only fluctuations of the gradient shape (Fig. 4F, see Fig. S4 in the supplementary material).

In summary, although showing some variability, the Dpp gradient is precise enough to provide positional information with a resolution of about two cells in a target tissue which is ~100 cells wide. These data also show that Dpp precision is not maximal in the cells adjacent to the source, but at a certain distance from the source. This is in qualitative agreement with our theoretical prediction of the relative concentration uncertainty (compare Fig. 2E with Fig. 4F). The fact that Dpp has maximal precision at a certain distance from the source indicates that both fluctuations of the morphogen flux from the source and cell-to-cell variability in the target tissue influence the gradient precision.

Precision of the Dpp activity gradient

In the previous sections, we analyzed the precision of the Dpp gradient and the theoretical constraints that determine the spatial precision profile. How is this precision conveyed downstream through the Dpp signaling pathway? Upon Dpp binding to its receptor, the transcription factor Mad is phosphorylated and imported into the nucleus, thereby initiating a signaling cascade that leads to the transcriptional activation of target genes through the repression of Brinker (Campbell and Tomlinson, 1999; Jazwinska et al., 1999; Kim et al., 1997; Newfeld et al., 1997). Consequently, the nuclear PMad concentration is a direct, early measure of the Dpp signaling activity.

We quantified the nuclear PMad concentration in the same disks in which we quantified the GFP-Dpp profiles using an anti-PMad antibody (Fig. 5A, Materials and methods). The PMad concentration decreases away from the Dpp source in an activity gradient $c^{PMad}(x)$, described by an exponential decay $\bar{c}^{PMad}(x)=P_0\exp(-x/\lambda^{PMad})$ where P_0 is the PMad level at x=0 (Fig. 5B). Analogous to GFP-Dpp, we determined the decay length of the PMad gradient (λ^{PMad}=25.2±4.5 μm=9.7±1.7 cells) and the total PMad level I^{PMad} (variation coefficient 0.24). The average λ^{PMad} is comparable to the average decay length of the Dpp gradient (λ^{Dpp}=17.0 μm=6.5 cells; Fig. 4C), supporting that the Dpp gradient is transduced downstream into a parallel activity gradient. Here we discuss normalized PMad profiles (Materials and methods), because the determination of PMad levels by immunostaining captures relative PMad levels within one disk, but does not permit one to reliably compare the overall levels from different disks. The nuclear PMad and the Dpp concentrations at the same distance from the source are correlated (correlation index R=0.69 for the non-normalized and R=0.76 and normalized Dpp data; Fig. 5C, see also Fig. S5 in the supplementary material). This is consistent with the notion that the PMad gradient is controlled by a fraction of the total Dpp level, implying that analysis of the total Dpp concentration can be used to estimate the Dpp pool actively engaged in signaling.

As for Dpp, we estimated the precision of the PMad gradient by determining the relative concentration uncertainty of PMad, $\Sigma^{PMad}(x)=\sigma_c^{PMad}(x)/\bar{c}^{PMad}(x)$, where $\sigma_c^{PMad}(x)$ is the uncertainty of c^{PMad} at a distance x (Fig. 5B inset). $\Sigma^{PMad}(x)$ is similar to the relative uncertainty of the Dpp concentration ($\Sigma^{Dpp}(x)$; see Fig. 5D versus Fig. 4F): both have similar values and exhibit a local minimum near the Dpp source. At the minimum of $\Sigma^{PMad}(x)$, the positional uncertainty of PMad $\sigma_x^{PMad}\cong\lambda^{PMad}\Sigma^{PMad}(x)=3.5\ \mu m = 1.4$ cells, i.e.

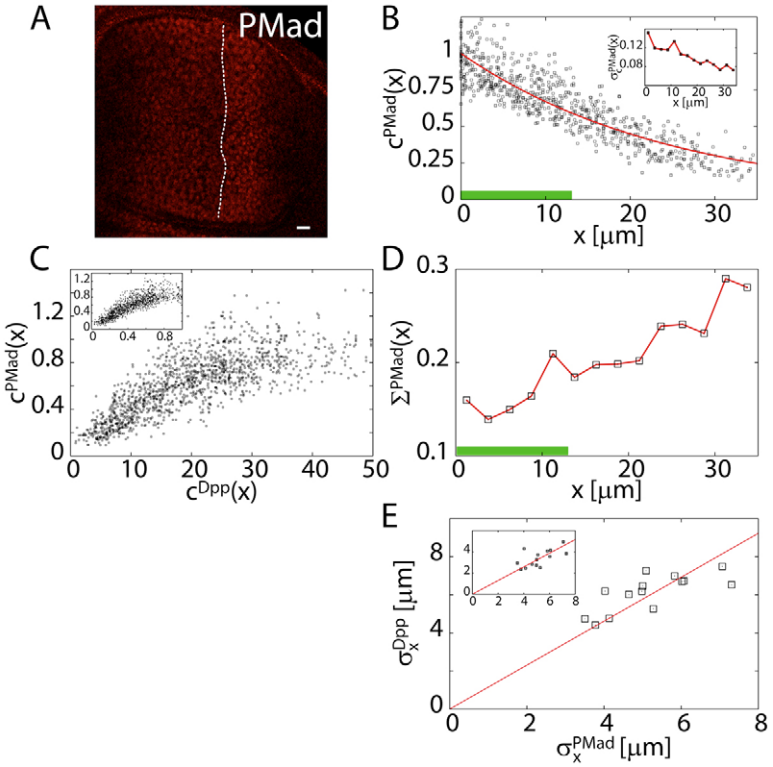

Fig. 5. Precision of the PMad gradient. (**A**) Immunostaining for PMad (red). Same set of disks, orientation, source boundary and scale bar as in Fig. 4A. (**B**) PMad FI in individual nuclei as a function of the distance x from the Dpp source, normalized to the total FI. The average PMad profile (red line) is approximated by an exponential function $c^{PMad}(x)=P_0\exp(-x/\lambda^{PMad})$ with λ^{PMad}=25.0 μm=9.6 cells. Inset, uncertainty $\sigma_c^{PMad}(x)$ of the FI. (**C**) Normalized PMad correlated to non-normalized GFP-Dpp level in the same disk and for the same position. Inset, the same but normalized GFP-Dpp data. (**D**) Relative concentration uncertainty $\Sigma^{PMad}(x)=\sigma_c^{PMad}(x)/c^{PMad}(x)$ of PMad. Note the similarity to Fig. 4F. (**E**) Positional uncertainty $\sigma_x^{PMad}(x)$ of the PMad gradient as a function of the positional uncertainty of the non-normalized GFP-Dpp gradient, $\sigma_x^{Dpp}(x)$. Inset, same but with normalized GFP-Dpp data. $\sigma_x^{PMad}(x)$ and $\sigma_x^{Dpp}(x)$ are proportional with a proportionality constant (slope of the red line) close to 1: $\sigma_x^{Dpp}\cong1.15\sigma_x^{PMad}$, non-normalized GFP-Dpp data, and $\sigma_x^{Dpp}(x)\cong0.65\sigma_x^{PMad}(x)$, normalized. Green horizontal bars in B,D, 5 cell diameters (13 μm).

it is about one cell diameter and on the order of the positional uncertainty of the Dpp gradient at this position. The positional uncertainty at different x of the Dpp gradient σ_x^{Dpp} is correlated to that of the PMad gradient σ_x^{PMad} (R=0.74 for the non-normalized and R=0.63 for the normalized Dpp data). The PMad gradient has a similar precision as the Dpp gradient, as indicated by a constant of proportionality for the two imprecisions that is close to one (Fig. 5E). These observations suggest that the precision of the Dpp gradient is maintained at the level of the downstream PMad activity gradient.

Precision of the Dpp target Spalt

Since a relatively precise Dpp concentration gradient is translated into a similarly precise Dpp activity gradient encoded in the phosphorylation state of Mad, we next asked how precise is the response of the Dpp target genes. The PMad-Medea protein complex binds directly to a silencer sequence in the *brinker* repressor gene (Müller et al., 2003). This way, the extracellular Dpp morphogen establishes a finely tuned, graded readout of transcriptional repression (reviewed by Affolter and Basler, 2007). The target gene *sal* is indeed expressed in response to the repression of Brinker occurring upon Dpp signaling, up to a distance x^* from the Dpp source (Fig. 6A) (Barrio and de Celis, 2004; Campbell and Tomlinson, 1999; Lecuit et al., 1996; Nellen et al., 1996). The spatial transition from *sal*-expressing to non-expressing cells is not perfectly step-like, but graded in a region of finite width (see below). Important questions are (1) whether the precision of the position x^* corresponds to the precision of the final wing vein pattern and (2) whether the precision of the position x^* is related to the precision of the Dpp and PMad gradients at x^*. It is noteworthy that Dpp, PMad, Sal and the final vein positioning represent only four steps in a complex cascade of events that guides wing patterning. In principle, precision of the final pattern could be affected in any step of this chain, such as by the distribution of the receptor Thickveins, the conversion of PMad-Medea to an inverse Brinker gradient, the control of *knirps* and *knirps-related* transcription by Sal, etc. (Jazwinska et al., 1999; Lecuit and Cohen, 1998; Lunde et al., 1998).

To address the patterning precision at the level of Dpp target genes, we determined the precision of the *sal* domain boundary in the same set of disks in which we analyzed the Dpp and PMad gradients. We determined the Sal FI profile as a function of the distance x to the Dpp source (Fig. 6B,C) and fitted a sigmoidal function $s(x)=s_0(\tanh((d-x)/w)+1)/2$ to each profile. At the distance d from the source, the Sal level does not decay abruptly, but transitions from a high to a low value within a region of width $2w$ (Fig. 6B). To describe the distance at which Sal is activated in response to Dpp, we operationally defined a Sal domain boundary position x^* as $x^*=d+w$. At $x=x^*$, $s(x)$ has dropped below 12% of its maximum value s_0 (Fig. 6B, Materials and methods).

The average range of *sal* expression in the posterior compartment is $\bar{x}^*=\langle x^*\rangle$=39.1±6.1 μm=15.0±2.3 cells. Unlike the decay lengths of the Dpp and PMad gradients, which only weakly correlate with the disk size L (R=0.14 and R=0.03, respectively), x^* is correlated to L (R=0.56). This indicates that whereas the *sal* domain scales with the size of the tissue, the decay lengths of the Dpp concentration and signaling activity gradients do not at the end of development.

In third-instar disks, the vein primordia form as narrow stripes of cells at the boundaries between different sectors of gene expression along the anterior-posterior axis (Biehs et al., 1998; Sturtevant et al., 1997; Sturtevant and Bier, 1995). Previous work has shown that the L2 vein primordium appears at the anterior edge of the *sal* domain, whereas the vein L3 differentiates at the anterior boundary of the Dpp source (Sturtevant et al., 1997). Sal then initiates a cascade of events that continues in the prepupal and pupal stages and leads to the final positioning and refinement of vein L2 in the adult wing (de Celis and Barrio, 2000; Lunde et al., 1998). The adult morphological vein pattern scales with wing size and is extremely precise. To compare the precision of the *sal* range in the disk to the precision of the vein

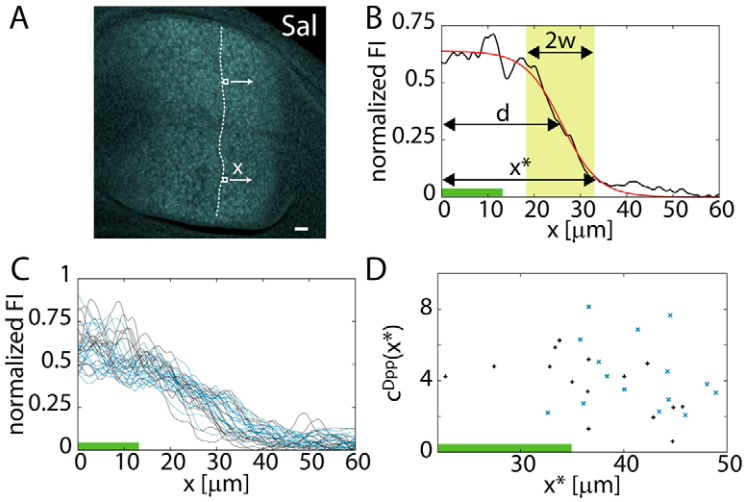

Fig. 6. Precision of the expression domain of the Dpp target gene *sal*. (**A**) Sal immunostaining. Same set of disks, orientation, source boundary and scale bar as in Fig. 4A. (**B**) The *sal* range $x^*=d+w$ was determined by fitting the sigmoidal function $s(x)=s_0(\tanh((d-x)/w)+1)/2$ (red line) to the Sal profile. Quantification and normalization as for GFP-Dpp (Fig. 4). (**C**) Sal profiles from the dorsal (black) and ventral compartments (blue). (**D**) Non-normalized Dpp concentration c^{Dpp} at x^* from the same wing disks in which x^* was determined. Dorsal profiles, black; ventral, blue. Green horizontal bars in B-D, 5 cell diameters (13 μm).

pattern in the adult wing, we measured the variability of the distance x_V between veins L2 and L3 in a set of 88 wings (see Materials and methods). This range corresponds approximately to the *sal* expression range in the wing primordium. We found that the variation coefficient of x_V in the adult wing (0.08) is smaller than that of x^* in the wing disk (0.16), indicating that the adult vein positioning is more invariable, regardless of organ size. This increased precision is even more obvious considering the *sal* range scaled to disk size and the distance between L2 and L3 scaled to the anterior-posterior length of the wing (variation coefficient 0.15 for the disk and 0.04 in the wing). Our data show that although x^* correlates to some extent with the size of the third-instar disk, later events in wing development (e.g. cell rearrangements, apoptosis) must contribute to the high precision of the final morphological pattern.

In a morphogen paradigm, the key question is whether the uncertainty of the *sal* domain position reflects the variability of the Dpp gradient, as would be expected for a Dpp target gene. The positional uncertainty of the Dpp gradient at the average *sal* boundary $\sigma_x^{Dpp}(\bar{x}^*)=\sigma_x^{Dpp}(39.1\ \mu m)\cong 9.7\ \mu m=3.7$ cells for the non-normalized Dpp concentrations and even lower ($\sigma_x^{Dpp}(\bar{x}^*)\cong 6.1\ \mu m=2.3$ cells) for the normalized data (Fig. 4F). Thus the imprecision of the Dpp gradient is similar to the variability of the Sal boundary position. This is indeed consistent with a morphogen paradigm in which the ligand concentration defines the target gene expression domains in a concentration-dependent manner (Wolpert, 1969).

It is in principle possible that the local Dpp level in a given disk determines the position of x^* with higher precision than three to four cells. In this scenario, the fluctuations in position of the Sal domain would result directly from the fluctuations of the Dpp level, and therefore correlate with them. If this is the case, we expect to find similar Dpp concentrations at the Sal boundary x^* regardless of the actual value of x^* in a particular disk. Fig. 6D shows that the dispersion of the concentrations of Dpp at distance x^* from the source corresponds to a positional uncertainty, which is not smaller than the three to four cells described above. This lack of clear correlation between the Dpp concentration and x^* is also related to the fact that the position of the *sal* boundary correlates with disk size, whereas the Dpp gradient does not. In summary, these observations imply that Dpp is able to convey positional information only with a precision of three to four cells in each disk, and that additional mechanisms must contribute to the accurate vein patterning.

DISCUSSION

Morphogen gradients provide cells in developing tissues with positional information that is used to form patterns of distinct cell types. As a consequence, adult animals have organs with precisely defined shapes and stereotypically patterned tissues. It is therefore important to ask if such precise patterns could be laid down by morphogen gradients. Alternatively, these gradients could lay out a relatively coarse pattern, while mechanisms occurring later in development increase precision. In this report, we addressed how cell-to-cell variability affects the precision of morphogen gradients. The transport of morphogens through a tissue with irregularly shaped cells with individual properties leads to an uncertainty in the shape of the resulting graded concentration profile. We have shown experimentally and theoretically that this uncertainty depends on the distance from the source in a characteristic way. The uncertainty of the positional information encoded in the Dpp gradient is lowest a few cells away from the source, where it is about one cell diameter. Closer to the source, precision is reduced by fluctuations of the morphogen production rate in the source, whereas farther away from the source fluctuations of the morphogen concentration accumulate as molecules move through the tissue.

Precision and dimensionality

We have shown that the precision of morphogen gradients rapidly increases with increasing tissue dimensionality (Fig. 3). We speculate that this might influence the 'choice' of dimensionality in different developmental contexts: mesenchyme versus epithelium versus linear arrays. For example, upon proximodistal patterning of the limb, digits first develop in two-dimensional primordia. Later, interdigital cells are eliminated by apoptosis leaving behind one-dimensional structures (Wolpert, 2002). According to our results, initiating the patterning in two-dimensional structures would help to circumvent the potential uncertainty that is characteristic to linear arrays.

Gradient precision and positional uncertainty

Our theory can explain the observed qualitative behavior of the gradient precision. It also implies that the magnitude of the observed concentration uncertainty could be caused by relative fluctuations of about 10% for the values of j, D and k in the source and the target tissue ($\sigma_j/j_0\cong 0.1$, $\sigma_D/D_0\cong 0.1$, $\sigma_k/k_0\cong 0.1$; see Fig. S2D in the supplementary material). However, two effects that are not

considered here might also contribute to the large observed uncertainty: additional sources of cell-to-cell variability and experimental noise.

First, theoretical analysis shows that the uncertainty of the total concentration is increased by a constant factor if a fraction of the observed GFP-Dpp is immobilized in endosomes. This is due to cell-to-cell variations in the rate of transfer to the immobile pool. Note, however, that correlations between the fluctuations of D and k can increase precision. Such correlations could occur in a scenario of active Dpp transport (Entchev et al., 2000), in which endocytosis mediates the movement of Dpp (i.e. its diffusion), but also controls its intracellular lysosomal degradation.

A second source of the large observed concentration uncertainty is background noise and measurement errors. Our inaccuracy of measurement is less than 2% of the Dpp fluorescence next to the source (Kicheva et al., 2007). However, far from the source, the signal to noise ratio is low, and therefore the experimentally determined concentration uncertainty exceeds the effects stemming from cell-to-cell variability. We consequently underestimate the precision of the Dpp gradient at greater distances from the source.

We can however use our theoretical results to obtain an estimate of the precision of the Dpp gradient at large distances. In a tissue such as the wing disk, our theory shows that the concentration uncertainty increases rather moderately as $\Sigma(x)\sim x^{1/4}$, which implies that the precision does not deteriorate dramatically within the range over which the morphogen signals. Assuming that Dpp signals up to $4\lambda^{Dpp}$=68 μm=26 cells away from its source, we estimate from the concentration uncertainty at $x=\lambda^{Dpp}$ that the positional uncertainty remains smaller than 3.5 cell diameters over the range of Dpp signaling (smaller than two cell diameters if we base this estimate on the normalized Dpp data).

Target precision and the morphogen model

In the case of the morphogen Bcd, it has been found that the gradient, which shows an embryo-to-embryo variability of the concentration at a certain position of ~10%, is transduced into *hb* activation with a similar imprecision of 10% (Gregor et al., 2007). This implies a positional precision of about a single cell diameter. For Dpp, we found that the uncertainty of the Sal range x^* is two to three cell diameters, which is similar to the positional uncertainty of the Dpp gradient at this distance to the source (Fig. 4F). This suggests that Dpp can convey the positional information required to position the Sal boundary with an accuracy of ~3 cells. Considering the Dpp gradient decay length (λ^{Dpp}=6.5 cells), two neighboring cells would have to discriminate a relative concentration difference of about 15% to respond with an accuracy of a single cell, which is comparable to the 10% reported for the Bcd gradient. This difference corresponds to about 65 GFP-Dpp molecules at the *sal* boundary [estimated using fluorescence/concentration calibration (Kicheva et al., 2007)]. Since the actual precision at the *sal* boundary is ~3 cells, this would require the ability of cells to discriminate a difference of at least ~200 molecules or 37% at the *sal* border. It is interesting to compare the implications of these numbers for Dpp and Bcd. It has been suggested that an averaging time of 2 hours might be required for a single cell to detect variations of the Bcd level of 10% (Gregor et al., 2007). This time results from the estimated slow kinetics of binding of the transcription factor to the DNA target site. Because this would be slow compared with the time scale for gene expression boundary formation in the embryo, which is in the order of minutes, spatial averaging has been invoked as a possible means to achieve precise readout (Gregor et al., 2007). In contrast to Bcd, several hundred receptors are available to detect Dpp ligands on the cell surface (Gurdon et al., 1994), which reduces the required time for averaging significantly. Furthermore, in the wing disk, establishment of target gene boundaries happens on longer time scales than in the embryo (hours or days as opposed to several minutes). Finally, we have shown that the Dpp readout precision is about 37%. Therefore, the observed kinetics and precision of Dpp are fully consistent with the positioning of target gene boundaries in the wing disk, and mechanisms other than readout of the Dpp concentration gradient over time would not need to be invoked.

The final vein pattern in the wing is more precise than three cells, implying that Dpp acts as a morphogen to coarsely provide positional information, which is refined by downstream events. Such events are known to occur later in development, during which dorsal to ventral signals and lateral inhibition contribute to the fine positioning and the final alignment of the veins on the two surfaces of the wing (Biehs et al., 1998; de Celis and Barrio, 2000; Lunde et al., 1998; Sturtevant and Bier, 1995).

Here it is important to mention that we analyzed both non-normalized and normalized FI profiles. The normalization (see Materials and methods) enabled us to separate variations of the gradient shape due to cell-to-cell variability from disk-to-disk variations of the overall gradient amplitude, reflecting the physiological variability which different animals experience in the culture. Similarly, our theory describes both fluctuations of the gradient shape and of the total Dpp level. The total FI (and therefore the Dpp concentration) in different disks indeed varies (variation coefficient 0.26). If the Dpp signal-transduction system in different disks responds identically to the same absolute concentrations of Dpp, the positional uncertainty conveyed by the Dpp gradient at the *sal* boundary would be 3.7, instead of 2.3 cell diameters.

Several scenarios are consistent with the idea that Dpp functions as a morphogen that provides information more accurate than three to four cell diameters. First, it could be that Dpp functions as an accurate morphogen that positions the boundaries of target genes such as *sal* precisely in earlier stages. At later stages, *sal* might respond to other cues or be maintained to some extent by lineage, which could explain the observed correlation of *sal* range with disk size. Second, Dpp could determine target gene expression precisely at and around the distance at which precision is highest and not at greater distances. In this scenario, Dpp would be a precise short-range, rather than long-range, morphogen. Although this is still unclear, we favor the former scenario. Alternatively, we also consider the possibility that Dpp is a morphogen with low precision, and other developmental mechanisms refine the coarse positional information it provides. In the future, it would be interesting to see whether this is a specific feature of *sal* or whether the same behavior can be seen for other target genes.

We thank all members of the M.G.-G. and F.J. groups for constructive criticism of the manuscript. This work was supported by the Max Planck Society, DFG, VW, EU, SNF and HFSP.

Supplementary material

Supplementary material for this article is available at
http://dev.biologists.org/cgi/content/full/135/6/1137/DC1

References

Affolter, M. and Basler, K. (2007). The Decapentaplegic morphogen gradient: from pattern formation to growth regulation. *Nat. Rev. Genet.* **8**, 663-674.
Arias, A. M. and Hayward, P. (2006). Filtering transcriptional noise during development: concepts and mechanisms. *Nat. Rev. Genet.* **7**, 34-44.
Barrio, R. and de Celis, J. F. (2004). Regulation of spalt expression in the Drosophila wing blade in response to the Decapentaplegic signaling pathway. *Proc. Natl. Acad. Sci. USA* **101**, 6021-6026.
Bergmann, S., Sandler, O., Sberro, H., Shnider, S., Schejter, E., Shilo, B.-Z. and Barkai, N. (2007). Pre-steady-state decoding of the bicoid morphogen gradient. *PLoS Biol.* **5**, e46.

Biehs, B., Sturtevant, M. A. and Bier, E. (1998). Boundaries in the Drosophila wing imaginal disc organize vein-specific genetic programs. *Development* **125**, 4245-4257.
Bollenbach, T., Kruse, K., Pantazis, P., González-Gaitán, M. and Jülicher, F. (2005). Robust formation of morphogen gradients. *Phys. Rev. Lett.* **94**, 018103.
Bollenbach, T., Kruse, K., Pantazis, P., González-Gaitán, M. and Jülicher, F. (2007). Morphogen tansport in epithelia. *Phys. Rev. E* **75**, 011901.
Briscoe, J. and Ericson, J. (1999). The specification of neuronal identity by graded Sonic Hedgehog signalling. *Semin. Cell Dev. Biol.* **10**, 353-362.
Campbell, G. and Tomlinson, A. (1999). Transducing the Dpp morphogen gradient in the wing of Drosophila: regulation of Dpp targets by brinker. *Cell* **96**, 553-562.
Capdevila, J., Pariente, F., Sampedro, J., Alonso, J. L. and Guerrero, I. (1994). Subcellular localization of the segment polarity protein patched suggests an interaction with the wingless reception complex in Drosophila embryos. *Development* **120**, 987-998.
Charpilienne, A., Nejmeddine, M., Berois, M., Parez, N., Neumann, E., Hewat, E., Trugnan, G. and Cohen, J. (2001). Individual rotavirus-like particles containing 120 molecules of fluorescent protein are visible in living cells. *J. Biol. Chem.* **276**, 29361-29367.
Colman-Lerner, A., Gordon, A., Serra, E., Chin, T., Resnekov, O., Endy, D., Pesce, C. G. and Brent, R. (2005). Regulated cell-to-cell variation in a cell-fate decision system. *Nature* **437**, 699-706.
Crauk, O. and Dostatni, N. (2005). Bicoid determines sharp and precise target gene expression in the Drosophila embryo. *Curr. Biol.* **15**, 1888-1898.
de Celis, J. F. and Barrio, R. (2000). Function of the spalt/spalt-related gene complex in positioning the veins in the Drosophila wing. *Mech. Dev.* **91**, 31-41.
de Celis, J. F., Barrio, R. and Kafatos, F. C. (1999). Regulation of the spalt/spalt-related gene complex and its function during sensory organ development in the Drosophila thorax. *Development* **126**, 2653-2662.
Driever, W. and Nüsslein-Volhard, C. (1988a). The bicoid protein determines position in the Drosophila embryo in a concentration-dependent manner. *Cell* **54**, 95-104.
Driever, W. and Nüsslein-Volhard, C. (1988b). A gradient of bicoid protein in Drosophila embryos. *Cell* **54**, 83-93.
Eldar, A., Dorfman, R., Weiss, D., Ashe, H., Shilo, B. Z. and Barkai, N. (2002). Robustness of the BMP morphogen gradient in Drosophila embryonic patterning. *Nature* **419**, 304-308.
Eldar, A., Rosin, D., Shilo, B. Z. and Barkai, N. (2003). Self-enhanced ligand degradation underlies robustness of morphogen gradients. *Dev. Cell* **5**, 635-646.
Elowitz, M. B., Levine, A. J., Siggia, E. D. and Swain, P. S. (2002). Stochastic gene expression in a single cell. *Science* **297**, 1183-1186.
Entchev, E. V., Schwabedissen, A. and González-Gaitán, M. (2000). Gradient formation of the TGF-beta homolog Dpp. *Cell* **103**, 981-991.
Ericson, J., Morton, S., Kawakami, A., Roelink, H. and Jessell, T. M. (1996). Two critical periods of Sonic Hedgehog signaling required for the specification of motor neuron identity. *Cell* **87**, 661-673.
González-Gaitán, M. (2003). Signal dispersal and transduction through the endocytic pathway. *Nat. Rev. Mol. Cell Biol.* **4**, 213-224.
Gregor, T., Bialek, W., de Ruyter van Steveninck, R. R., Tank, D. W. and Wieschaus, E. F. (2005). Diffusion and scaling during early embryonic pattern formation. *Proc. Natl. Acad. Sci. USA* **102**, 18403-18407.
Gregor, T., Tank, D. W., Wieschaus, E. F. and Bialek, W. (2007). Probing the limits to positional information. *Cell* **130**, 153-164.
Gurdon, J. B., Harger, P., Mitchell, A. and Lemaire, P. (1994). Activin signalling and response to a morphogen gradient. *Nature* **371**, 487-492.
Houchmandzadeh, B., Wieschaus, E. and Leibler, S. (2002). Establishment of developmental precision and proportions in the early Drosophila embryo. *Nature* **415**, 798-802.
Houchmandzadeh, B., Wieschaus, E. and Leibler, S. (2005). Precise domain specification in the developing Drosophila embryo. *Phys. Rev. E* **72**, 061920.
Howard, M. and ten Wolde, P. R. (2005). Finding the center reliably: robust patterns of developmental gene expression. *Phys. Rev. Lett.* **95**, 208103.
Jaeger, J., Surkova, S., Blagov, M., Janssens, H., Kosman, D., Kozlov, K. N., Manu, Myasnikova, E., Vanario-Alonso, C. E., Samsonova, M. et al. (2004). Dynamic control of positional information in the early Drosophila embryo. *Nature* **430**, 368-371.
Jazwinska, A., Kirov, N., Wieschaus, E., Roth, S. and Rushlow, C. (1999). The Drosophila gene brinker reveals a novel mechanism of Dpp target gene regulation. *Cell* **96**, 563-573.
Kicheva, A., Pantazis, P., Bollenbach, T., Kalaidzidis, Y., Bittig, T., Jülicher, F. and González-Gaitán, M. (2007). Kinetics of morphogen gradient formation. *Science* **315**, 521-525.
Kim, J., Johnson, K., Chen, H. J., Carroll, S. and Laughon, A. (1997). Drosophila Mad binds to DNA and directly mediates activation of vestigial by Decapentaplegic. *Nature* **388**, 304-308.
Kimmel, C. B., Ullmann, B., Walker, M., Miller, C. T. and Crump, J. G. (2003). Endothelin 1-mediated regulation of pharyngeal bone development in zebrafish. *Development* **130**, 1339-1351.
Kruse, K., Pantazis, P., Bollenbach, T., Jülicher, F. and González-Gaitán, M. (2004). Dpp gradient formation by dynamin-dependent endocytosis: receptor trafficking and the diffusion model. *Development* **131**, 4843-4856.
Kühnlein, R. P., Frommer, G., Friedrich, M., González-Gaitán, M., Weber, A., Wagner-Bernholz, J. F., Gehring, W. J., Jäckle, H. and Schuh, R. (1994). spalt encodes an evolutionarily conserved zinc finger protein of novel structure which provides homeotic gene function in the head and tail region of the Drosophila embryo. *EMBO J.* **13**, 168-179.
Lander, A. D., Nie, Q. and Wan, F. Y. (2002). Do morphogen gradients arise by diffusion? *Dev. Cell* **2**, 785-796.
Lecuit, T. and Cohen, S. M. (1998). Dpp receptor levels contribute to shaping the Dpp morphogen gradient in the Drosophila wing imaginal disc. *Development* **125**, 4901-4907.
Lecuit, T., Brook, W. J., Ng, M., Calleja, M., Sun, H. and Cohen, S. M. (1996). Two distinct mechanisms for long-range patterning by Decapentaplegic in the Drosophila wing. *Nature* **381**, 387-393.
Lunde, K., Biehs, B., Nauber, U. and Bier, E. (1998). The knirps and knirps-related genes organize development of the second wing vein in Drosophila. *Development* **125**, 4145-4154.
Moser, M. and Campbell, G. (2005). Generating and interpreting the Brinker gradient in the Drosophila wing. *Dev. Biol.* **286**, 647-658.
Müller, B., Hartmann, B., Pyrowolakis, G., Affolter, M. and Basler, K. (2003). Conversion of an extracellular Dpp/BMP morphogen gradient into an inverse transcriptional gradient. *Cell* **113**, 221-233.
Nellen, D., Burke, R., Struhl, G. and Basler, K. (1996). Direct and long-range action of a DPP morphogen gradient. *Cell* **85**, 357-368.
Newfeld, S. J., Mehra, A., Singer, M. A., Wrana, J. L., Attisano, L. and Gelbart, W. M. (1997). Mothers against dpp participates in a DDP/TGF-beta responsive serine-threonine kinase signal transduction cascade. *Development* **124**, 3167-3176.
Raser, J. M. and O'Shea, E. K. (2005). Noise in gene expression: origins, consequences, and control. *Science* **309**, 2010-2013.
Strigini, M. (2005). Mechanisms of morphogen movement. *J. Neurobiol.* **64**, 324-333.
Sturtevant, M. A. and Bier, E. (1995). Analysis of the genetic hierarchy guiding wing vein development in Drosophila. *Development* **121**, 785-801.
Sturtevant, M. A., Biehs, B., Marin, E. and Bier, E. (1997). The spalt gene links the A/P compartment boundary to a linear adult structure in the Drosophila wing. *Development* **124**, 21-32.
Tabata, T. and Takei, Y. (2004). Morphogens, their identification and regulation. *Development* **131**, 703-712.
Tanimoto, H., Itoh, S., ten Dijke, P. and Tabata, T. (2000). Hedgehog creates a gradient of DPP activity in Drosophila wing imaginal discs. *Mol. Cell* **5**, 59-71.
Teleman, A. A. and Cohen, S. M. (2000). Dpp gradient formation in the Drosophila wing imaginal disc. *Cell* **103**, 971-980.
Wolpert, L. (1969). Positional information and the spatial pattern of cellular differentiation. *J. Theor. Biol.* **25**, 1-47.
Wolpert, L. (2002). *Principles of Development*. Oxford: Oxford University Press.

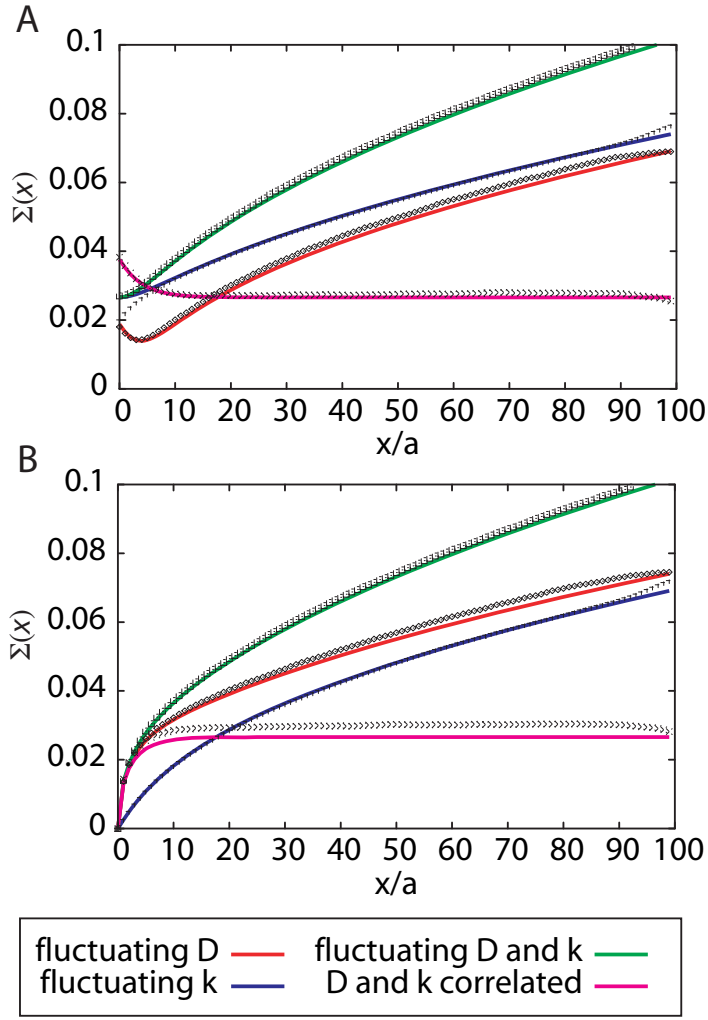

Fig. S1. Relative uncertainty Σ(*x*) of the steady state concentration *c(x)* for the diffusion-degradation model with disorder in one dimension (1). (**A**,**B**) The symbols indicate results from numerical calculations in which steady-state gradients were calculated for many (typically 100,000) realizations of the disorder. The lines show the corresponding analytical results (8) for Σ(*x*). The red lines show Σ(*x*) if only *D* is fluctuating, the blue lines if only *k* is fluctuating, the green lines if both *D* and *k* are fluctuating, and the magenta lines if *D* and *k* are fluctuating in a fully correlated way. In A, the current *j* is imposed at *x*=0. In B, the concentration *c* is imposed at *x*=0. Parameters are $\lambda / a = \sqrt{50}$, $\sigma_j / j_0 = \sigma_{c_0} / c_0 = 0$, $\sigma_D / D_0 = \sigma_k / k_0 = 0.1$. In the fully correlated case $2\rho_{kD} / k_0 D_0 = (\sigma_D / D_0)^2 + (\sigma_k / k_0)^2$ while ρ_{kD}=0 otherwise. A Gaussian distribution was used for the noise terms in the numerical calculations. Steady states were calculated on a linear chain of size 100*a*.

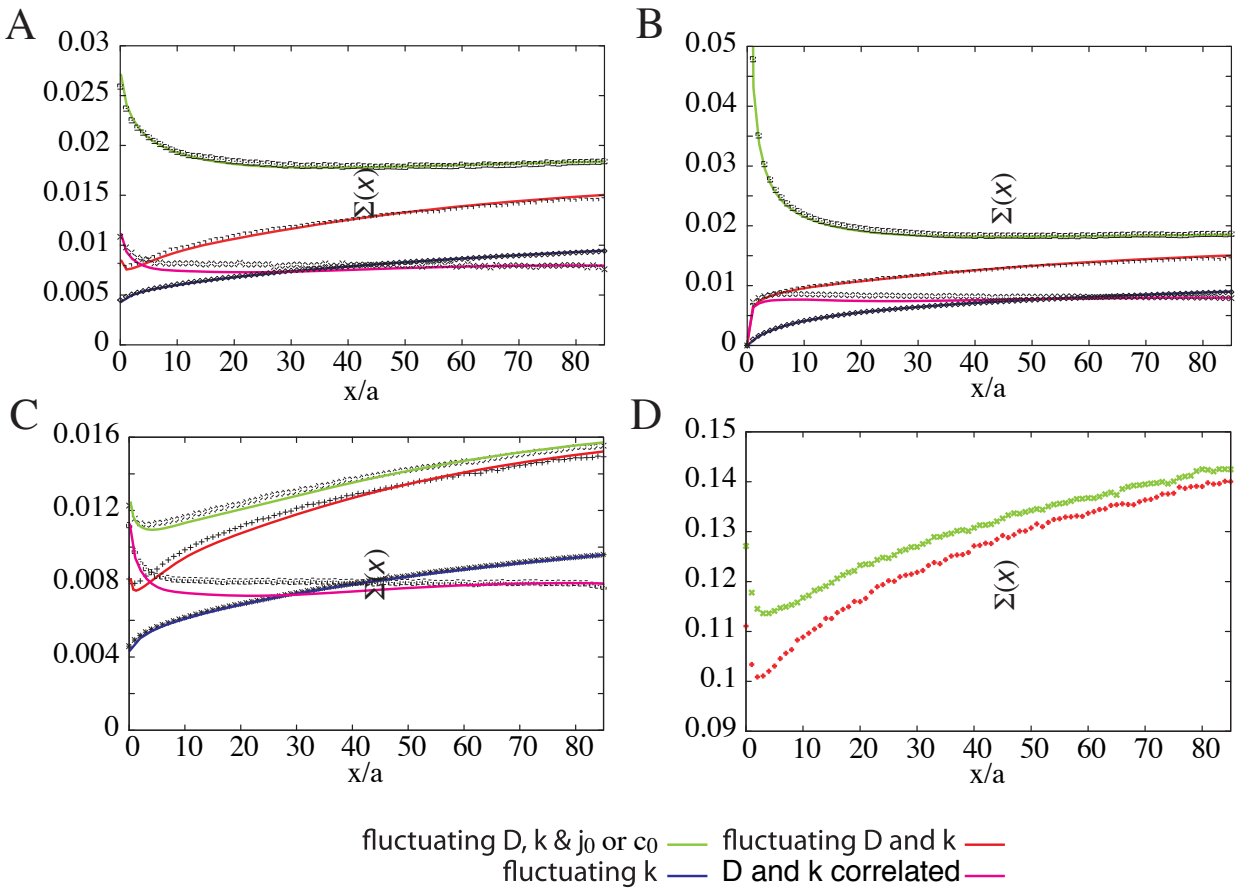

Fig. S2. Relative uncertainty Σ(*x*) of the steady state concentration *c(x)* for the diffusion-degradation model with disorder in two dimensions. The symbols indicate results from numerical calculations in which steady-state gradients were calculated for many (typically 100,000) realizations of the disorder. The lines show the corresponding analytical results for Σ(*x*) that follow from (10). The blue lines show Σ(*x*) if only *k* is fluctuating, the red lines if both *D* and *k* are fluctuating, the magenta line if *D* and *k* are fluctuating in a fully correlated way, and the green lines if *D*, *k* and the respective quantity imposed at the boundary at $x=0$ (j or c_0) are fluctuating. (**A**) Relative concentration uncertainty Σ(*x*) with the current *j* imposed at $x=0$. (**B**) Σ(*x*) with the concentration c_0 imposed at $x=0$. (**C**) Like A, but with parameters corresponding to Fig. 2 of the main manuscript. (**D**) Relative concentration uncertainty Σ(*x*) for the general case in which the hopping rates between two neighboring sites in opposite direction are uncorrelated. Current *j* imposed at $x=0$. Compared to A-C, the magnitude of Σ(*x*) is increased in this situation. Parameters as in Fig. S1, with $\sigma_j / j_0 = \sigma_{c_0} / c_0 = 0.1$ in A,B, $\sigma_j / j_0 = 0.037$ in C, $\sigma_j / j_0 = 0.25$ in D, and $\lambda / a = 7$ in C,D. A Gaussian distribution was used for the noise terms in the numerical calculations. Steady states were calculated on a simple cubic lattice of size $100a \times 100a$.

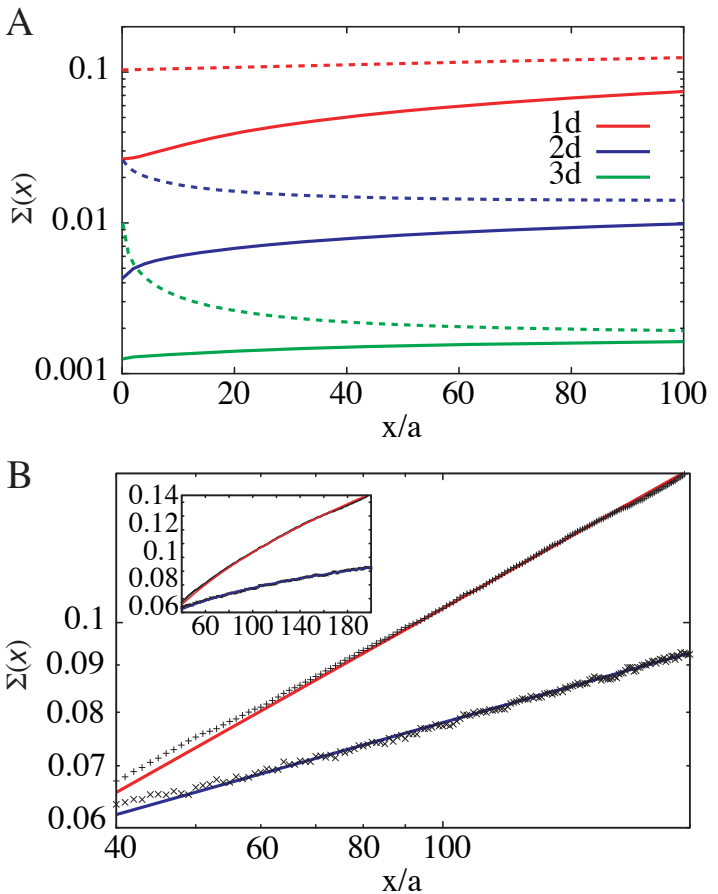

Fig. S3. Relative concentration uncertainty $\Sigma(x)$ for the diffusion-degradation model with disorder for different space dimensionalities. All calculations were done with j imposed at x=0. (**A**) Logarithmic plot of $\Sigma(x)$ in one dimension (red lines), in two dimensions (blue lines), and in three dimensions (green lines). For the solid lines, only k is fluctuating and for the broken lines both k and j are fluctuating. Shown are the analytical results for $\Sigma(x)$ given by (8), (10) and (12) for the different space dimensionalities respectively. (**B**) Double-logarithmic plot of $\Sigma(x)$ for large x in one and two dimensions. In these calculations, k and D are fluctuating. Numerical results are shown by symbols. In two dimensions, $\Sigma(x)$ was multiplied by a factor of five. For comparison, functions proportional to $x^{1/2}$ and $x^{1/4}$ are shown in red and blue, respectively. The inset shows the same data using linear axes. Parameters as in Fig. S1 with $\sigma_j / j_0 = 0.1$ and $\rho_{kD} = 0$. Steady states in two dimensions were calculated on a simple cubic lattice of size $220a \times 100a$.

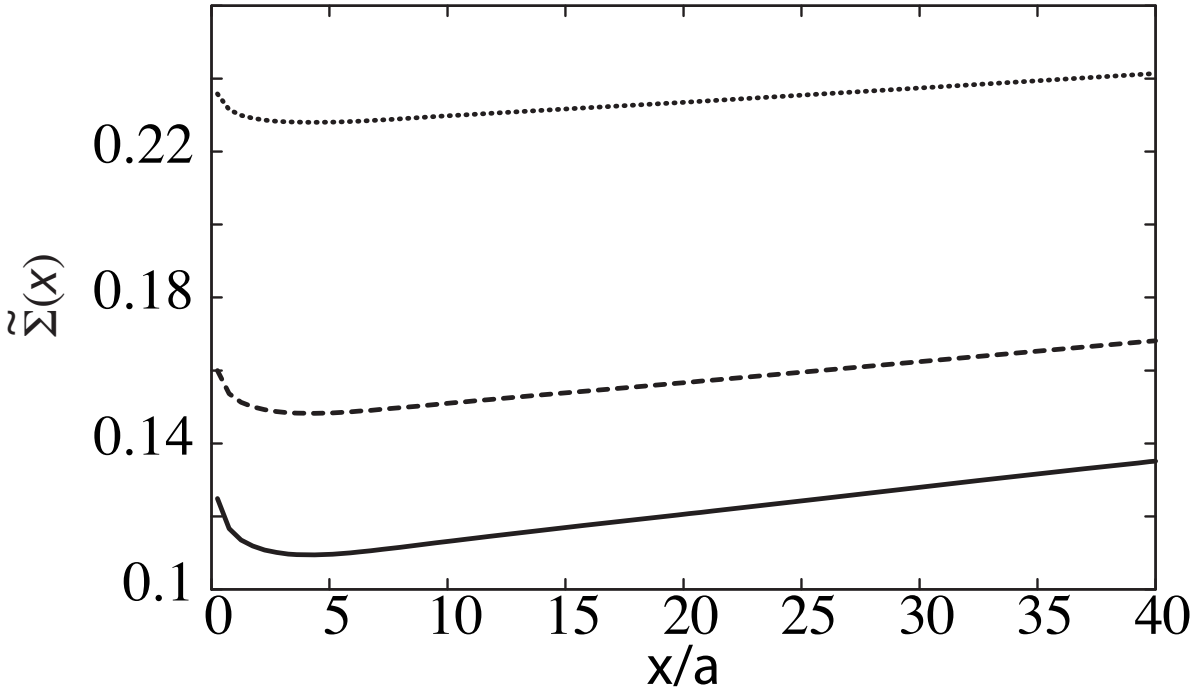

Fig. S4. Relative concentration uncertainty $\tilde{\Sigma}(x)$ in presence of disk-to-disk variations of the current imposed at x=0. For the solid line $\sigma_{j_0} / j_0^0 = 0$, for the dashed line $\sigma_{j_0} / j_0^0 = 0.1$, and for the dotted line $\sigma_{j_0} / j_0^0 = 0.2$. Remaining parameters as in Fig. 2 of the main manuscript.

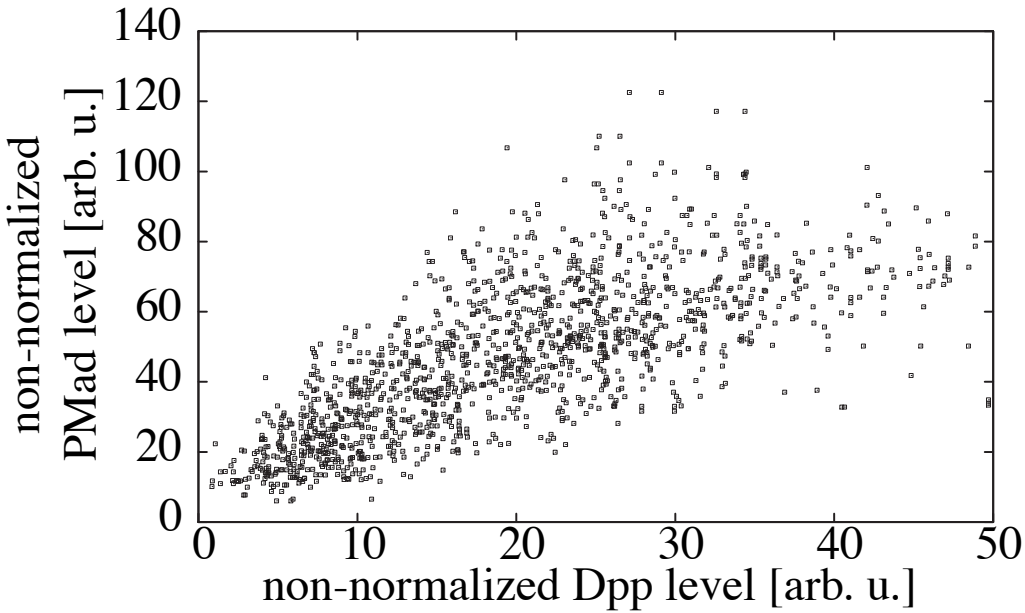

Fig. S5. Correlations between PMad and Dpp concentrations. Non-normalized PMad level of all nuclei shown in Fig. 5B of the main manuscript correlated with the non-normalized GFP-Dpp level at the same distance from the source in the same wing disk (R=0.63). Compare with Fig. 5C of the main manuscript, which shows the same plot for the normalized PMad data. These data were obtained from a set of N=15 wing disks from *dpp* mutants rescued by a GFP-Dpp transgene using the UAS/Gal4 driver system.

I. THEORETICAL DESCRIPTION OF MORPHOGEN TRANSPORT IN A TISSUE WITH CELL-TO-CELL VARIABILITY

We introduce cell-to-cell variability as random components to the diffusion coefficient and the degradation rate in the diffusion-degradation equation which describes the time evolution of the morphogen concentration profile, see equation (1) in the experimental procedure of the main manuscript. This is done most naturally in a discrete description. We consider a lattice with sites corresponding to individual cells. In one dimension, the morphogen concentration on site n is denoted C_n, with $n = 0, 1, 2, \ldots$. Molecules are transported to neighboring sites with rates p_n^+ (from site n to $n+1$) and p_n^- (for the transport from $n+1$ to n). In addition, molecules on site n are degraded with a rate k_n. Cell-to-cell variability leads to variations of the rates $p_n^\pm$ and k_n as a function of n. To keep our discussion simple, we restrict ourselves to the simpler situation where $p_n = p_n^+ = p_n^-$, i.e. transport in opposite directions between cells occurs at the same rate p_n.

The concentrations C_n satisfy the kinetic equation

$$\partial_t C_n = p_{n-1}(C_{n-1} - C_n) + p_n(C_{n+1} - C_n) - k_n C_n, \quad \text{for } n > 0, \tag{1}$$

where $\partial_t = \partial/\partial t$. The lattice begins at site $n = 0$ corresponding to the morphogen source. Two different boundary conditions are considered: fixed concentration C_0^0 and a morphogen source at $n = 0$ emitting morphogens at an imposed rate ν. The concentration C_0 then satisfies

$$\partial_t C_0 = \nu + p_0(C_1 - C_0) - k_0 C_0. \tag{2}$$

This discrete description can be generalized to square (or cubic) lattices in two and three dimensions (see Fig. 3 of the main manuscript).

In the absence of disorder (cell-to-cell variability) $p = p_n$ and $k = k_n$ are the same for all sites. On large scales, the concentrations follow a diffusion-degradation equation $\partial_t c = D\nabla^2 c - kc$ with $D = pa^2$ and degradation rate k. Here, $c(x) = C_n$ with $x = an$. Cell-to-cell variability corresponds to a situation where $p_n = p + \eta_n$ and $k_n = k + \zeta_n$. Here, η_n and ζ_n are random variables with zero average. They are characterized by their correlators which we choose to be $\langle \eta_n \eta_j \rangle = \sigma_D^2/a^4 \delta_{nj}$ and $\langle \zeta_n \zeta_j \rangle = \sigma_k^2 \delta_{nj}$. Here, the brackets $\langle \ldots \rangle$ denote an ensemble average over all realizations of the random variables. These relations imply that the values of η_n and ζ_n at different bonds of the lattice are uncorrelated. The η_n and ζ_n can

also be correlated at each lattice site: $\langle \eta_n \zeta_j \rangle = \rho_{kD}/a^2 \delta_{nj}$.

In addition to the rates p_n and k_n, the rate of ligand influx into the system ν can be fluctuating, i.e. $\nu = \nu_0 + \chi$ where χ is a random variable with $\langle \chi \rangle = 0$, $\langle \chi^2 \rangle = \sigma_j^2/a^2$, and $\langle \chi \eta_n \rangle = \langle \chi \zeta_n \rangle = 0$ for all $n \geq 0$. In the case of a fixed concentration at $n = 0$, one can introduce fluctuations at the boundary very similarly: $C_0 = C_0^0 + \gamma$ with a random variable γ satisfying $\langle \gamma \rangle = 0$, $\langle \gamma^2 \rangle = \sigma_{c_0}^2$, and $\langle \gamma \eta_n \rangle = \langle \gamma \zeta_n \rangle = 0$. The standard deviations σ_D/a^2, σ_k, σ_j/a, and σ_{c_0} of the noise terms η_n, ζ_n, χ, and γ are assumed to be small compared to the mean values p, k, ν_0, and C_0^0 respectively. Our discussion is mostly independent of the specific probability distributions of η_n, ζ_n, χ, and γ. It is only required that these distributions are tightly localized around their mean value zero.

II. CONTINUUM LIMIT

In the presence of disorder, the kinetics of the concentration field can be described on large scales in a continuum limit. In d dimensions, with $\vec{x}$ describing a position in space, i.e. $\vec{x} = (x, y)$ in $d = 2$ and $\vec{x} = (x, y, z)$ in $d = 3$, the concentration field $c(t, \vec{x})$ obeys

$$\partial_t c(t, \vec{x}) = \nabla \cdot \left[(D_0 + \eta(\vec{x})) \, \nabla c(t, \vec{x}) \right] - (k_0 + \zeta(\vec{x})) \, c(t, \vec{x}) \tag{3}$$

Here $\eta(\vec{x})$ and $\zeta(\vec{x})$ denote noise terms with zero average and correlators $\langle \eta(\vec{x}) \eta(\vec{x}') \rangle = \sigma_D^2 a^d \delta(\vec{x} - \vec{x}')$, $\langle \zeta(\vec{x}) \zeta(\vec{x}') \rangle = \sigma_k^2 a^d \delta(\vec{x} - \vec{x}')$, and $\langle \eta(\vec{x}) \zeta(\vec{x}') \rangle = \rho_{kD} a^d \delta(\vec{x} - \vec{x}')$. These correlators express the continuum limits of the expressions introduced in the discrete case. The amplitude of the fluctuations of D is σ_D and accordingly σ_k for k. A possible correlation of the fluctuations of D and k at a given position is measured by ρ_{kD}.

The fluctuations of the secretion rate of the source cells located at $x < 0$ are captured by imposing a current

$$(D_0 + \eta(\vec{x})) \, \partial_x c(\vec{x}, t) \Big|_{x=0} = -j_0 - \chi(\vec{x}) \Big|_{x=0} \tag{4}$$

across the boundary surface at $x = 0$, where $\chi(\vec{x})$ is a noise term with $\langle \chi(\vec{x}) \chi(\vec{x}') |_{x=0} \rangle = \sigma_j^2 a^{(d-1)} \delta^{(d-1)}(\vec{x} - \vec{x}')|_{x=0}$.

A. Effects of disorder on steady state gradients

The steady state solutions $c(\vec{x})$ of (3) depend on the particular realization of the disorder, reflecting the effects of cell-to-cell variability. The average gradient $\bar{c}(x) = \langle c(\vec{x}) \rangle$ is given by

an ensemble average over all possible realizations of the disorder. Alternatively, in a two-dimensional geometry with a line source at $x = 0$, the average gradient can be determined by averaging along the y direction for given x in a single realization of the disorder.

We first discuss the problem in $d = 1$. It is assumed that the amplitude of the noise is small, i.e. $\sigma_D/D_0 \ll 1$ and $\sigma_k/k_0 \ll 1$. We calculate the variance of the concentration

$$\sigma_c^2(x) = \langle (c(x) - \bar{c}(x))^2 \rangle \tag{5}$$

by using a perturbation expansion to first order in the small parameters σ_D/D_0 and σ_k/k_0. Note that to first order the average concentration is given by $\bar{c}(x) = c_0 e^{-x/\lambda}$ where $\lambda = \sqrt{D_0/k_0}$ is the diffusion length and $c_0 = j_0/\sqrt{k_0 D_0}$.

The results of this calculation can be expressed in terms of Green's functions $G(x, x')$ of the linear operator $(D_0\partial_x^2 - k_0)$ which satisfy $(D_0\partial_x^2 - k_0)G(x, x') = \delta(x - x')$. To satisfy the two different boundary conditions at $x = 0$, two Green's functions $G_\pm(x, x')$ with $G_-(0, x') = 0$ and $\partial_x G_+(x, x')|_{x=0} = 0$ respectively are needed. In one dimension these functions are given by

$$G_\pm(x, x') = \frac{-1}{2\sqrt{k_0 D_0}} \left(e^{-|x-x'|/\lambda} \pm e^{-(x+x')/\lambda} \right). \tag{6}$$

To first order in our perturbation expansion, the variance of the concentration is given by

$$\begin{aligned} \langle \sigma_c^\pm(x)^2 \rangle \;=\; & D_0^2 \left(\partial_{x'} G_\pm(x, x') \Big|_{x'=0} \right)^2 \sigma_{c_0}^2 + G_\pm(x, 0)^2 \sigma_j^2 \\ & + a \int_0^\infty dx' \Big(\sigma_D^2 \bar{c}'(x')^2 (\partial_{x'} G_\pm(x, x'))^2 + \sigma_k^2 G_\pm(x, x')^2 \bar{c}(x')^2 \\ & + 2\rho_{kD} G_\pm(x, x') \bar{c}(x') \bar{c}'(x') \partial_{x'} G_\pm(x, x') \Big). \end{aligned} \tag{7}$$

Here, we use a condensed notation for both choices of the boundary condition at $x = 0$: σ_c^+ denotes the solution for a fixed current and σ_c^- the solution for a fixed concentration at $x = 0$. Using the explicit expressions for the Green's functions and $\bar{c}(x)$, this integral can be solved and expressed in terms of elementary functions. As discussed in the main text, a dimensionless measure of the relative concentration uncertainty at x is

$$\Sigma(x) = \frac{\left\langle (c(x) - \bar{c}(x))^2 \right\rangle^{1/2}}{\bar{c}(x)} = \frac{\langle \sigma_c(x)^2 \rangle^{1/2}}{\bar{c}(x)}.$$

Using (7), one obtains to first order in perturbation theory

$$\Sigma^\pm(x) \;=\; \left(\Sigma_B^\pm(x)^2 + \Sigma_k^\pm(x)^2 + \Sigma_D^\pm(x)^2 + \Sigma_{kD}^\pm(x) \right)^{1/2}, \text{ with}$$

$$
\begin{aligned}
\Sigma_B^+(x)^2 &= \left(\frac{\sigma_j}{j_0}\right)^2 \\
\Sigma_B^-(x)^2 &= \left(\frac{\sigma_{c_0}}{c_0}\right)^2 \\
\Sigma_k^\pm(x)^2 &= \frac{a}{8\lambda}\left(\frac{\sigma_k}{k_0}\right)^2\left(1 \pm 2 \mp e^{-2x/\lambda} + \frac{2x}{\lambda}\right) \\
\Sigma_D^\pm(x)^2 &= \frac{a}{8\lambda}\left(\frac{\sigma_D}{D_0}\right)^2\left(1 \mp 2 \pm 3e^{-2x/\lambda} + \frac{2x}{\lambda}\right) \\
\Sigma_{kD}^\pm(x) &= \frac{a}{4\lambda}\frac{\rho_{kD}}{k_0 D_0}\left(1 \pm e^{-2x/\lambda} - \frac{2x}{\lambda}\right).
\end{aligned} \tag{8}
$$

As the relative concentration fluctuations become arbitrarily large for large x, these results are only valid in a finite region $0 \le x \le M$ for some $M > 0$.

The steady state of (3) for $d = 2$ can be calculated iteratively as in the one dimensional situation. The free Green's function for the operator $(D_0(\partial_x^2 + \partial_y^2) - k_0)$ satisfying $(D_0(\partial_x^2 + \partial_y^2) - k_0)G_0(\vec{x}, \vec{x}') = \delta(\vec{x} - \vec{x}')$ is

$$
G_0(\vec{x}, \vec{x}') = \frac{-1}{2\pi D_0} K_0(|\vec{x} - \vec{x}'|/\lambda),
$$

where K_0 is a modified Bessel function of the second kind [1]. Using a mirror image technique, one can construct Green's functions $G_\pm(\vec{x}, \vec{x}')$ that satisfy $G_-(\vec{x}, \vec{x}')|_{x=0} = 0$ and $\partial_x G_+(\vec{x}, \vec{x}')|_{x=0} = 0$ respectively:

$$
G_\pm(x, y, x', y') = G_0(x, y, x', y') \pm G_0(x, y, -x', y'). \tag{9}
$$

To first order, the variance of $c(\vec{x})$ is

$$
\begin{aligned}
\langle \sigma_c^\pm(\vec{x})^2 \rangle &= a\int_{-\infty}^{\infty} dy' \left(\sigma_{c_0}^2 D_0^2 \left(\partial_{x'} G_\pm(\vec{x}, \vec{x}')\Big|_{x'=0}\right)^2 + \sigma_j^2 G_\pm(x, y, 0, y')^2\right) \\
&\quad + a^2 \int_0^\infty dx' \int_{-\infty}^{\infty} dy' \Big(\sigma_k^2 G_\pm(\vec{x}, \vec{x}')^2 \bar{c}(x')^2 + \sigma_D^2 \bar{c}'(x')^2 (\partial_{x'} G_\pm(\vec{x}, \vec{x}'))^2 \\
&\quad + 2\rho_{kD} \bar{c}(x') \bar{c}'(x') G_\pm(\vec{x}, \vec{x}') \partial_{x'} G_\pm(\vec{x}, \vec{x}')\Big).
\end{aligned} \tag{10}
$$

The resulting relative concentration uncertainty grows asymptotically as $\Sigma(x) = \langle \sigma_c(\vec{x})^2 \rangle^{1/2} / \bar{c}(x) \sim x^{1/4}$. The first term in (10) is due to the fluctuations of the current across the boundary line at $x = 0$ or the concentration that is fixed there. This term alone decreases as $\Sigma(x) \sim x^{-1/4}$ for large x. Positive correlations between the fluctuations of k_0 and D_0 increase the precision as in the one dimensional case.

One can calculate the standard deviation of the concentration in $d = 3$ as well. We are interested in the steady state solution of (3) with $\vec{x} = (x, y, z)$ and $\nabla = (\partial_x, \partial_y, \partial_z)$ in the

half-space $x \geq 0$. Either the concentration or the current is imposed on the boundary plane $x = 0$, i.e. $c(\vec{x})|_{x=0} = c_0 + \gamma(y, z)$ or $\partial_x c(\vec{x})|_{x=0} = -D_0^{-1}(j_0 + \chi(y, z))$.

The Green's functions for the two boundary conditions at $x = 0$ can again be constructed:

$$G_\pm(\vec{x}, \vec{x}') = \frac{-1}{4\pi D_0}\left(\frac{e^{-r/\lambda}}{r} \pm \frac{e^{-r_m/\lambda}}{r_m}\right), \tag{11}$$

with $r = ((x - x')^2 + (y - y')^2 + (z - z')^2)^{1/2}$ and $r_m = ((x + x')^2 + (y - y')^2 + (z - z')^2)^{1/2}$. The result for the variance of $c(\vec{x})$ to first order in perturbation theory is

$$\begin{aligned}\langle \sigma_c^\pm(\vec{x})^2 \rangle \;=\; & a^2 \int_{-\infty}^{\infty} dy' \int_{-\infty}^{\infty} dz' \left(\sigma_{c_0}^2 D_0^2 \left(\partial_{x'} G_\pm(\vec{x}, \vec{x}')\right)^2 + \sigma_j^2 G_\pm(\vec{x}, \vec{x}')^2\right)\Big|_{x'=0} \\ & + a^3 \int_0^{\infty} dx' \int_{-\infty}^{\infty} dy' \int_{-\infty}^{\infty} dz' \Big(\sigma_k^2 G_\pm(\vec{x}, \vec{x}')^2 \bar{c}(x')^2 + \sigma_D^2 \bar{c}'(x')^2 (\partial_{x'} G_\pm(\vec{x}, \vec{x}'))^2 \\ & + 2\rho_{kD} \bar{c}(x') \bar{c}'(x') G_\pm(\vec{x}, \vec{x}') (\partial_{x'} G_\pm(\vec{x}, \vec{x}'))\Big).\end{aligned} \tag{12}$$

We have integrated (12) numerically. The resulting relative concentration uncertainty $\Sigma(x)$ is shown in Suppl. Fig. 3 A for a fixed current at the boundary. Asymptotically, $\Sigma(x) \sim \ln(x)$. The contribution from the boundary term alone decreases asymptotically as $\Sigma(x) \sim x^{-1/2}$.

B. Effects of disk-to-disk variations of the morphogen secretion rate

As discussed in the main text, the total fluorescence intensity (FI) of the non-normalized GFP-Dpp FI profiles measured experimentally varies considerably from disk-to-disk. This is most likely due to variations in the secretion rate of morphogens from the source cells between wing disks from different larvae.

Such disk-to-disk variations can easily be included in our theoretical description. In addition to the cell-to-cell fluctuations which are already taken into account in (4), we assume that the current imposed at $x = 0$ fluctuates with a standard deviation σ_{j_0} about its mean value j_0^0 for different gradients in our ensemble. We further assume that these fluctuations are not correlated with any of the cell-to-cell fluctuations in the system. The relative concentration uncertainty $\tilde{\Sigma}(x)$ that takes disk-to-disk variations of the morphogen secretion rate into account is then

$$\tilde{\Sigma}(x) = \sqrt{(\sigma_{j_0}/j_0^0)^2 + \Sigma(x)^2}, \tag{13}$$

where $\Sigma(x)$ is the relative concentration uncertainty in the absence of disk-to-disk variations of the morphogen secretion rate which was calculated above. In Suppl. Fig. 4, we show

$\tilde{\Sigma}(x)$ for different values of σ_{j_0}. While the behavior of $\tilde{\Sigma}(x)$ is qualitatively the same as that of $\Sigma(x)$, the minimum of $\tilde{\Sigma}(x)$ is less and less pronounced in relative terms for increasing values of σ_{j_0}.

III. NUMERICAL SIMULATIONS

We have performed numerical calculations of the discrete description (1) for the two different boundary conditions at $x = 0$ in one and two dimensions. At the remaining boundaries, we imposed zero flux boundary conditions. A large number of steady state gradients was calculated for different realizations of the disorder using a Gaussian distribution for the random variables. From these, the average value and standard deviation of C_n at all lattice sites n were calculated. The resulting relative concentration uncertainty is shown in Suppl. Fig. 1 for the different boundary conditions in $d = 1$ and in Suppl. Fig. 2 for $d = 2$. A good agreement with the results of the perturbative calculation is found.

Furthermore, we have numerically calculated the relative concentration uncertainty $\Sigma(x)$ in the general case in which the rates of transfer in opposite directions between neighboring sites are uncorrelated. In one dimension this implies $p_n^+ \neq p_n^-$ (Fig. 1C of the main manuscript). Suppl. Fig. 2D shows that while the qualitative features of $\Sigma(x)$ remain the same in this situation, the uncertainty is about an order of magnitude larger than in the case $p_n^+ = p_n^-$ for the same noise amplitude $\sigma_D/D_0 = 0.1$. This implies that the values of $\Sigma(x)$ are comparable to those observed experimentally.

---

[1] E. Weisstein, *Mathworld*, http://mathworld.wolfram.com/, wolfram Research, Inc.

Table S1. Average values and variability of the key quantities discussed in the main text

Quantity	Mean value [μm]	Standard deviation [μm]	Variation coefficient
GFP-Dpp decay length λ^{Dpp}	17.0	4.3	0.26
PMad decay length λ^{PMad}	25.2	4.5	0.18
Sal range x^*	39.1	6.1	0.16
Wing disk size L	132.6	21.0	0.16

These results were obtained from a set of N=15 wing disks from *dpp* mutants rescued by a GFP-Dpp transgene using the UAS/Gal4 driver system.

Table S2. Correlation indices *R* of the key quantities discussed in the main text

	λ^{Dpp}	λ^{PMad}	x^*	L	I^{Dpp}
λ^{PMad}	–0.04				
x^*	0.39	0.49			
L	0.14	0.03	0.56		
I^{Dpp}	0.13	0.30	0.26	–0.22	
I^{PMad}	0.18	0.33	0.58	0.55	0.29

The strongest correlations are observed between the disk size L and Sal range x^*, the total PMad level I^{PMad} and x^* and between I^{PMad} and L. These results were obtained from a set of N=15 wing disks from *dpp* mutants rescued by a GFP-Dpp transgene using the UAS/Gal4 driver system.